Detailed chemical compositions of planet-hosting stars: II. Exploration of the interiors of terrestrial-type exoplanets

H. S. Wang, S. P. Quanz, D. Yong, F. Liu, F. Seidler, L. Acuña, S. J. Mojzsis

Monthly Notices
of the
ROYAL ASTRONOMICAL SOCIETY

MNRAS **513,** 5829–5846 (2022)
Advance Access publication 2022 April 25

https://doi.org/10.1093/mnras/stac1119

Detailed chemical compositions of planet-hosting stars – II. Exploration of the interiors of terrestrial-type exoplanets

H. S. Wang [1,2]★ S. P. Quanz [1,2] D. Yong [3] F. Liu [4] F. Seidler [1] L. Acuña [5] and S. J. Mojzsis [6,7,8]

[1] *Institute for Particle Physics and Astrophysics, ETH Zürich, Wolfgang-Pauli-Strasse 27, CH-8093 Zürich, Switzerland*
[2] *National Center of Competence in Research PlanetS (www.nccr-planets.ch), Switzerland*
[3] *Research School of Astronomy and Astrophysics, Australian National University, Canberra, ACT 2611, Australia*
[4] *Centre for Astrophysics and Supercomputing, Swinburne University of Technology, Hawthorn, Victoria 3122, Australia*
[5] *Aix-Marseille Univ., CNRS, CNES, LAM, F- 13388, Marseille, France*
[6] *Origins Research Institute, Research Centre for Astronomy and Earth Sciences, MTA Centre of Excellence, H-1112 Budapest, Hungary*
[7] *Department of Lithospheric Research, University of Vienna, A-1090 Vienna, Austria*
[8] *Department of Geological Sciences, University of Colorado, Boulder, CO 80309-0399, USA*

Accepted 2022 April 19. Received 2022 April 15; in original form 2021 October 6

ABSTRACT

A major goal in the discovery and characterization of exoplanets is to identify terrestrial-type worlds that are similar to (or otherwise distinct from) our Earth. Recent results underscore the importance of applying devolatilization – i.e. depletion of volatiles – to the chemical composition of planet-hosting stars to constrain bulk composition and interiors of terrestrial-type exoplanets. In this work, we apply such an approach to a selected sample of 13 planet-hosting Sun-like stars, for which high-precision photospheric abundances have been determined in the first paper of the series. With the resultant devolatilized stellar composition (i.e. the model planetary bulk composition), as well as other constraints including mass and radius, we model the detailed mineralogy and interior structure of hypothetical, habitable-zone terrestrial planets ('exo-Earths') around these stars. Model output shows that most of these exo-Earths are expected to have broadly Earth-like composition and interior structure, consistent with conclusions derived independently from analysis of polluted white dwarfs. Exceptions are the Kepler-10 and Kepler-37 exo-Earths, which we predict are strongly oxidized and thus would develop metallic cores much smaller than Earth. Investigating our devolatilization model at its extremes as well as varying planetary mass and radius (within the terrestrial regime) reveals potential diversities in the interiors of terrestrial planets. By considering (i) high-precision stellar abundances, (ii) devolatilization, and (iii) planetary mass and radius holistically, this work represents essential steps to explore the detailed mineralogy and interior structure of terrestrial-type exoplanets, which in turn are fundamental for a quantitative understanding of planetary dynamics and long-term evolution.

Key words: planets and satellites: composition – planets and satellites: interiors – planets and satellites: terrestrial planets – stars: abundances.

1 INTRODUCTION

An important threshold is being crossed for detailed studies of interior structure and composition of terrestrial exoplanets following the ever more precise measurements of both planetary mass and radius (Weiss et al. 2016; Stassun, Collins & Gaudi 2017; Stassun et al. 2018; Otegi, Bouchy & Helled 2020) and of host stellar photospheres that reveal the primordial elemental compositions of the systems (Nissen 2015; Brewer & Fischer 2016; Liu et al. 2016, 2020; Delgado Mena et al. 2017; Bedell et al. 2018; Adibekyan et al. 2021; Clark et al. 2021). Indeed, the past decade has witnessed a number of interior models that follow this lead (e.g. Dorn et al. 2015; Santos et al. 2015; Unterborn, Dismukes & Panero 2016; Brugger et al. 2017; Dorn et al. 2017; Unterborn et al. 2018; Wang et al. 2019b; Acuna et al. 2021; Wang et al. 2022). We can anticipate that future observations of planetary atmospheres with *JWST* (Morley et al. 2017; Gialluca et al. 2021) and other innovative ground- and space-based missions and mission concepts such as ELT/METIS (Quanz et al. 2015; Bowens et al. 2021), ARIEL (Tinetti et al. 2018; Turrini et al. 2021), PLATO (Rauer et al. 2014; Nascimbeni et al. 2022), and LIFE (Quanz et al. 2021, 2022) will reveal new details of the surface and interior characteristics of terrestrial exoplanets, given the evolutionary outcomes of the dynamic interactions between the interior, surface, atmosphere, and possible hydrosphere or even biosphere (Bower et al. 2019; Shahar et al. 2019; Ortenzi et al. 2020; Acuna et al. 2021; Dyck, Wade & Palin 2021; Hakim et al. 2021; Kacar, Garcia & Anbar 2021).

In the present work, we build upon the procedures outlined in Wang, Lineweaver & Ireland (2019a) and Wang et al. (2019b) (W19a and b, thereafter) that introduced the idea of using *devolatilized* host stellar abundances, rather than the *uncorrected* host stellar abundances, to constrain the bulk composition and interior modelling of hypothetical habitable-zone terrestrial exoplanets ('exo-Earths'). This idea was established based on the observations of bulk composition differences and similarities of the Solar system's rocky bodies relative to the Sun (Grossman & Larimer 1974; Bland et al.

★ E-mail: haiwang@phys.ethz.ch

2005; Davis 2006; Carlson et al. 2014; Sossi & Fegley 2018; Wang, Lineweaver & Ireland 2018). Importantly, among the 10 major rock-forming elements (Mg, Si, Fe, Ni, Al, Ca, Na, O, S, and C), only Ca and Al (the two most refractory ones) are not observed to be depleted in rocky bodies relative to the Sun. All other elements on this list have been depleted to some degree: e.g. for Mg, Si, Fe, and Ni the depletion is by ∼10–20 per cent; for volatiles like O, S, and C the depletion is over 80 per cent (W19a). It is reasonable to argue that the devolatilization process is not unique to the Solar system and may be a universal process in the formation of rocky (exo)planets. A recent study of the major rock-forming elements (including oxygen) for a sample of six white dwarfs (Doyle et al. 2019) shows that the bulk composition of the planetary debris polluting these stellar core remnants resembles those of rocky planets in the Solar system. This suggests that the parent rocky bodies of these pollutants must also be devolatilized relative to their host stars (also see Bonsor et al. 2021; Harrison, Shorttle & Bonsor 2021), although the exact devolatilization factors for such planetary systems are beyond what can be constrained with the existing data. Hence, starting with the best-known calibration of the devolatilization based on our Solar system (in particular, Sun and Earth; W19a), we can apply it, to first order, to other Sun-like star systems and estimate the potential rocky planetary bulk composition from the measurable host stellar photospheric abundances. Subsequently, planetary interior composition and structure can be modelled, as shown for a sample of four planet-hosting stars in W19b. Even further, interior dynamics and thermo-chemical evolution (Spaargaren et al. 2020, 2021; Wang et al. 2020b), carbon cycle modelling (Hakim et al. 2021), and habitability arguments (Kacar et al. 2021) ensue from such an analysis.

Here, we extend the analysis to a further sample of 13 planet-hosting Sun-like stars for which detailed and precise chemical compositions (for up to 18 elements including all major rock-forming elements at a typical precision of ∼0.025 dex) have been determined with high-quality spectra in the first paper of the series (Liu et al. 2020; hereafter Paper I). We are interested in how diverse the interiors of the model exo-Earths around these stars would be.

The paper is organized by presenting our methodology and analysis in Section 2 and results in Section 3, followed by a discussion of the effect of varying devolatilization scaling factors (within plausible bounds) and planetary size (within the terrestrial regime) on the interiors and of the model restrictions in Section 4. We summarize and conclude in Section 5.

2 METHODOLOGY AND ANALYSIS

2.1 Methodology

To carry out the analysis, two sets of software are employed: EXOINT (W19b) for devolatilizing stellar abundances and modelling stoichiometric mantle and core compositions as well as core mass fractions (CMFs); and, PERPLE_X (Connolly 2009) for modelling of a detailed mantle mineralogy and interior structure (e.g. self-consistent density, pressure, and temperature profiles, as well as core radius fraction). It is important to note that the devolatilization model of W19a that we adopted is empirically quantified by the bulk elemental abundance ratio (f) between Earth and proto-Sun as a function of 50 per cent condensation temperature (T_c; Lodders 2003):

$$\log(f) = \alpha \log(T_c) + \beta \quad (1)$$

where, the best-fitting coefficients are $\alpha = 3.676 \pm 0.142$ and $\beta = -11.556 \pm 0.436$.

Application of such a model to other planetary systems is by all means a simplification of devolatilization processes and outcomes that may vary across different systems and, in principle, even at different orbital distances within one system. We therefore limit such application to habitable-zone, terrestrial-type exoplanets around Sun-like stars – i.e. exo-Earths by our definition. It has been shown in the literature (e.g. Sossi & Fegley 2018; Wang 2018; Yoshizaki & McDonough 2020) that the bulk compositional differences of Venus and Mars from the Sun are within the uncertainty of such a difference between Earth and Sun. We emphasize that the empirical devolatilization model of W19a is the first-order quantitative model of such an important process. A sophisticated, forward model of devolatilization that involves disc evolution, accretion, and hydrodynamic escape processes is still awaiting formalization (e.g. Wang 2022). To account for potential variation in devolatilization scales for the exo-Earths considered here, we vary the uncertainty range of the adopted W19a model arbitrarily by a factor of 3 to assess how this may affect the interior modelling results (to be discussed in Section 4.1).

For the detailed procedure of EXOINT, we refer the reader to Fig. 3 and appendix A of W19b. It is briefly summarized here that we adopt the chemical networks of Na_2O-CaO-MgO-Al_2O_3-SiO_2-FeO-NiO-SO_3-CO_2-C(graphite/diamond)-metals for the mantle composition (in terms of first-order oxides and reduced phases) and of Fe-Ni-Si-S alloy for the core composition of a terrestrial-type exoplanet. The CMF is determined by mass balance after distributing the bulk planetary composition into the stoichiometric mantle and core compositions. The difference to W19b is that Si is not first oxidized in the oxidation sequence of major elements, but follows Na, Ca, Mg, and Al and precedes Fe, Ni, and S. This approach allows for the possibility that Si can be partially oxidized in the case of a reduced mantle (i.e. at a low oxidation state) and comports with the fact that it can be an important light element constituent of metallic cores (McDonough 2003; Hirose, Labrosse & Hernlund 2013; Li & Fei 2014; Wang et al. 2018). This update has been applied in Wang et al. (2022) and the code is publicly accessible.[1]

Having determined stoichiometric mantle and core compositions, as well as CMFs, planetary mineralogy (i.e. complex mineral assemblages) and structure are then modelled with PERPLE_X by assuming that these exo-Earths are all Earth-like in mass and radius. Later in the discussion (Section 4.2), we explore the effect of varied planetary mass and radius (within the terrestrial density regime) on the predictions of detailed interiors. The underlying method for computing mantle mineralogy, given the mantle composition of major oxides and the pressure and temperature profiles for a terrestrial-type planet, is Gibbs-free energy minimization (Connolly 2009). The mineral equations of state and thermodynamic parameters – essential for the Gibbs-free energy minimization – are adopted from Stixrude & Lithgow-Bertelloni (2011). For a given Fe-Ni-Si-S-alloy core, we adopt the equation of state from Kuwayama et al. (2020). We adopt an adiabatic thermal gradient, as similarly practiced in Dorn et al. (2015), Unterborn et al. (2018), and Lorenzo (2018), and integrate it with a mantle potential temperature of 1700 K at 1 bar, arbitrarily set to be approximate to that of the modern Earth (Anderson 2000). Hinkel & Unterborn (2018) found that different setups of a mantle potential temperature (at a typical range of 1500 and 1900 K) for a terrestrial-type planet only introduce accountable effects towards the mineralogies in the transition zone

[1] https://github.com/astro-seanwhy/ExoInt/tree/master/v1.2 (IDL version); https://github.com/astro-seanwhy/ExoInt/tree/master/pyExoInt (Python version).

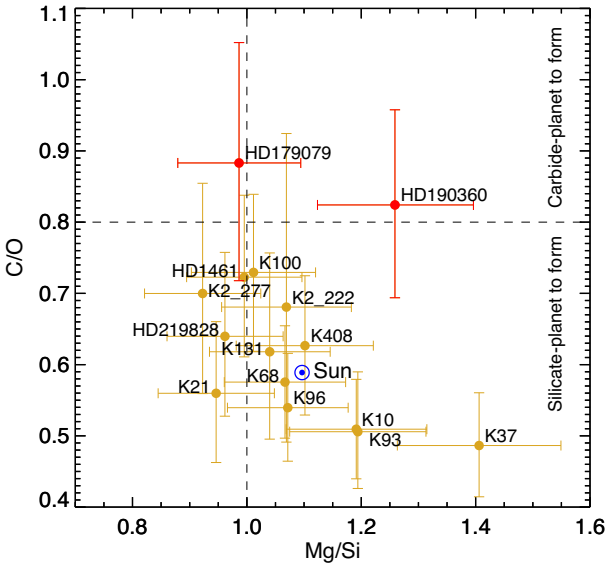

Figure 1. C/O versus Mg/Si – abundance ratios by number – for the sample of stars. The vertical and horizontal dashed lines, respectively, indicate the critical value of Mg/Si (= 1.0) and C/O (= 0.8; Bond, O'Brien & Lauretta 2010; Suárez-Andrés et al. 2018). HD179079 and HD190360 (coloured in red), for which C/O > 0.8, are excluded from our detailed analysis. The Sun ('⊙'; Asplund, Amarsi & Grevesse 2021) is shown for reference.

between the upper and lower mantle – we have verified this finding with Earth as an example (Fig. B1). We also introduce a temperature jump at the core mantle boundary (CMB) by following Noack & Lasbleis (2020; for all of these exo-Earths) and Stixrude (2014; for the tested cases with masses out of [0.8, 2]$M_\oplus$ – the range in which the Noack & Lasbleis (2020) model is parametrized). It was found that a variable thermal profile plays a negligible role in changing the interior structure (Dorn et al. 2015) – we have further verified this finding with varied temperature jumps at the CMB in the case of Earth (Fig. B2).

2.2 Sample selection and analysis

Our sample for this study is based on the planet-hosting stars studied in Paper I: Kepler-21, Kepler-37, Kepler-68, Kepler-93, Kepler-96, Kepler-K100, Kepler-131, K2-222 (EPIC220709978), K2-277 (EPIC212357477), Kepler-408, HD1461, and HD219828. The addition to this list is Kepler-10, for which the detailed elemental abundances are obtained in Liu et al. (2016) in the same fashion as in Paper I. We have excluded Kepler-409 because its oxygen abundance – essential for our analysis – is undetermined. We have also excluded HD179079 and HD190360, for which the values of C/O are larger than 0.8 (Fig. 1) and thus around which carbide planets may develop (Bond et al. 2010; Teske et al. 2014; Brewer & Fischer 2016). Our model is based on silicate chemistry and thus does not apply to plausible carbide planets. For the reader interested in the interiors of carbide planets, we refer to Hakim, van Westrenen & Dominik (2018) and Hakim et al. (2019) for more details. Therefore, we have a sample of 13 Sun-like stars (with 5400 $< T_{\rm eff} <$ 6400 K, 4.0 $< \log g <$ 4.5 cm s^{-2}, and $-0.3 <$ [Fe/H] $< +0.3$), each of which has been confirmed to host at least one planet with a mass $<10\,M_\oplus$ (except for HD 219828 that hosts a planet with a minimum mass of $\sim$21 $M_\oplus$). Since these detected planets are all in the proximity (with an orbital period <50 d) of their host stars, they are not included in this study that focuses on hypothetical, (habitable-zone) exo-Earths.

As shown in Fig. 1, the values of Mg/Si (abundance ratio by number) in our sample are distributed within a narrow range from $\sim$0.9 to $\sim$1.4. Mg/Si modulates the dominant mineral phases in the mantle of a silicate planet: pyroxene ($MgSiO_3$) and various feldspars for Mg/Si < 1, a mixture of olivine (Mg_2SiO_4) and pyroxene assemblages for 1 < Mg/Si <2, and olivine with other Mg-rich species for Mg/Si > 2 (Bond et al. 2010; Suárez-Andrés et al. 2018). At first glance, therefore, the mantles of exo-Earths around our sample of stars would most likely be made of a mixture of olivine and pyroxene assemblages, while some (with Mg/Si < 1) may be slightly enriched in pyroxenes.

Following the study of W19b, we apply the Sun-to-Earth devolatilization model (W19a) to the sample of stars for 10 major rock-forming elements: Mg, Si, Fe, Ni, Al, Ca, Na, O, S, and C. The differential abundances determined in Paper I (their table 2) are first converted to the absolute abundances by referring to the latest solar abundances of Asplund et al. (2021). We ignore the diffusion effect since this effect is equivalent for those major rock-forming elements for the Sun (Asplund et al. 2009) and presumably for Sun-like stars as well. We also do not consider the effect of Galactic chemical evolution (GCE) on the host stellar abundances, since planets are fundamentally correlated with the properties (and formation environment) of *individual* host stars. In other words, whatever a GCE effect may have with the host stellar abundances should have also been an inherent part of the formation histories of planets around these stars. Thus, the GCE effect has *validly* shaped the chemical compositions of these planets. The resultant, 'devolatilized' stellar abundances – i.e. the model planetary bulk composition – are listed in Table A1 and used as a principal set of constraints for a detailed modelling of the interiors of (hypothetical) exo-Earths around these stars.

3 RESULTS

3.1 Key planetary geochemical ratios

The abundance ratio of carbon to oxygen (hereafter C/O) in a planet host star is useful, as illustrated in Fig. 1, to indicate to first order if a potential rocky world around it would be dominated by silicates or by carbides. However, upon the application of the devolatilization, both oxygen and carbon become so severely depleted that the remaining atoms are principally locked in planetary mineral assemblages. C/O in a rocky planet is therefore no longer a valid indicator of the mantle oxidation state, which, however, is essential to understand the planetary interiors.

For a silicate planet including our own, MgO and SiO_2 are the foremost mineral oxides in the mantle, with Fe being distributed between its oxidized form (e.g. FeO) in the mantle and its reduced, metallic/liquid iron phase in the core, depending on the oxygen fugacity (fO_2) of the planet (McDonough & Sun 1995; Palme & O'Neill 2014; Dorn et al. 2015; Wang et al. 2019b). The calculation of fO_2, often relative to either the quartz-faylite-magnetite buffer (O'Neill 1987; Cottrell & Kelley 2011) or the iron-wüstite buffer (e.g. Doyle et al. 2019), requires the prior knowledge of the relative fractions between different phases of iron, which we do not have in the first place for exoplanets. Based on the estimated bulk elemental composition (Table A1) and considering that O, Mg, Si, and Fe are the foremost abundant, rock-forming elements (Palme & O'Neill 2014; Wang et al. 2018), we propose the bulk (O-Mg-2Si)/Fe as a

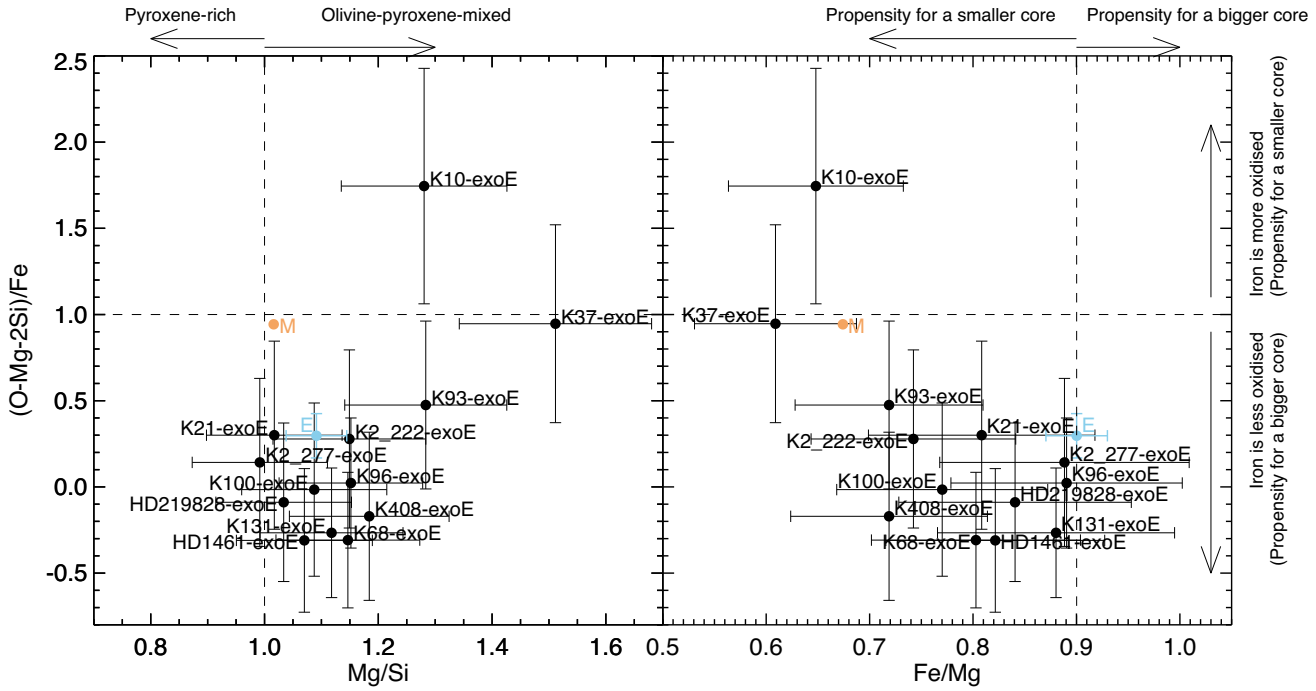

Figure 2. (O - Mg - 2Si)/Fe versus Mg/Si and (O - Mg - 2Si)/Fe versus Fe/Mg diagrams for the sample of model exo-Earths. The dashed, vertical, and horizontal lines classify these planets into different categories, in which different planetary interior properties may be expected (see text as well as the brief notations on the plot). Earth ('E', the blue dot; Wang et al. 2018) and Mars ('M', the brown dot; Yoshizaki & McDonough 2020) are shown for reference.

simple alternative of oxygen fugacity to indicate the oxidation state of a silicate terrestrial exoplanet.

Planetary Mg/Si (having no significant difference from its host stellar Mg/Si) is still critical to modulate the dominant mineral assemblages (olivine versus pyroxene) in the mantle of a silicate planet. Further, Fe/Mg is preferred over Fe/Si as an indicator of the degree of core-mantle fractionation (determining the core size), owing to the fact that Si may be present as a major light element in the core of a rocky planet (McDonough 2003; Hirose et al. 2013; Li & Fei 2014; Wang et al. 2018) and is indeed considered in the core compositional model in this work.

Fig. 2 shows the distributions of these model exo-Earths on the diagram of (O - Mg - 2Si)/Fe versus Mg/Si and (O - Mg - 2Si)/Fe versus Fe/Mg. First, it shows that all of the sample planets are significantly below the unit line of (O - Mg - 2Si)/Fe, except Kepler-10 exo-Earth ('K10-exoE') and Kepler-37 exo-Earth ('K37-exoE'). The direct implication is that most of these planets would have a large iron core and potentially an Earth-like structure while iron in K10-exoE and K37-exoE may be much more oxidized and thus these two planets would develop comparably smaller cores. The core size of K10-exoE would be the smallest due to its significantly high (O - Mg - 2Si)/Fe that would cause most of the iron to be oxidized and locked in the mantle. Considering that the core size is also modulated by Fe/Mg (right-hand panel of Fig. 2), K37-exoE – which has the equivalent oxidation state as Mars, but lower Fe/Mg – would potentially develop a core that is smaller, in relative terms, than the core:mantle ratio of Mars. Frank, Meyer & Mojzsis (2014) referred to this class of terrestrial-type exoplanets as 'Super-Lunas'. Among those planets clumped around the Earth's loci on both panels of the diagram, their mantle mineralogies would be more or less the same, with K93-exoE being likely the most olivine-rich due to its relatively high Mg/Si. These qualitative analyses are further verified by the following, detailed interior modelling.

3.2 Mantle and core compositions and core mass fraction

Our estimates of the mantle composition for all studied exo-Earths are presented in Table B1, with the normalized composition of the foremost major oxides (i.e. normalizing the sum of SiO_2, MgO, and FeO to be 100 wt per cent) shown in the ternary diagram Fig. 3. Overall, the mantle compositions of these exo-Earths are very similar, except for K10-exoE and K37-exoE. The latter two are particularly enriched in FeO, consistent with the analysis above based on key geochemical ratios.

The estimates of core composition and CMF (i.e. the core-to-planet mass ratio) of these exo-Earths are also presented in Table B1. We find that the core compositions of these exo-Earths are more or less the same, with the concentration of Fe ranging from ∼80 to ∼90 wt per cent. In contrast, the values of CMF are diverse, ranging from ∼0 to ∼40 wt per cent (Fig. 4). K10-exoE and K37-exoE, for which the concentrations of FeO in the mantle are the highest (as mentioned above), are the ones with the lowest CMFs – $0.0^{+9.4}_{-0.0}$ and $11.9^{+15.0}_{-11.9}$ – broadly mimicking Moon-like and Mars-like structures, respectively. The CMFs of eight exo-Earths (K21-exoE, K93-exoE, K96-exoE, K100-exoE, K408-exoE, K2-222-exoE, K2-227-exoE, and HD219828) are consistent with the CMF (32.5 ± 0.3 wt per cent; Wang et al. 2018) of the Earth within uncertainties. The remaining three exo-Earths (K68-exoE, K131-exoE, and HD 1461-exoE) have CMFs statistically higher than that of the Earth, with K131-exoE – appearing at the bottom right (i.e. with the highest Fe/Mg and lowest (O-Mg-2Si)/Fe) in the right-hand panel of Fig. 2 – being the highest ($39.7^{+4.4}_{-4.7}$ wt per cent).

The minor oxides – Na_2O, CaO, and Al_2O_3 – will be combined with the aforementioned three major oxides to model the detailed mineralogy of these exo-Earths. Other minor/trace end-members, including NiO, SO_3, CO_2, C and metals, are, however, not involved in the subsequently detailed interior modelling but their realization

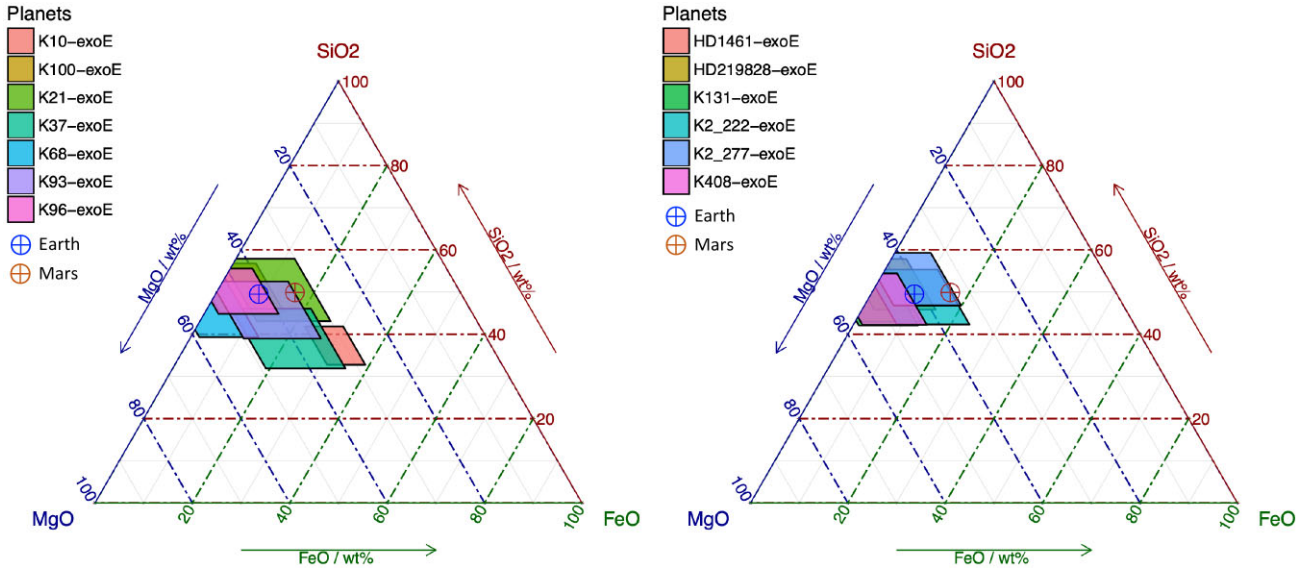

Figure 3. Ternary diagrams showing the estimated mantle compositions of major mineral oxides (normalized by SiO2 + MgO + FeO = 100 wt per cent) for the sample of model exo-Earths (for clarity, the sample is divided arbitrarily to two groups). The range of the quadrilaterals indicates the modelled 1σ uncertainties in the normalized mantle compositions of the individual planets. The normalized compositions of SiO2, MgO, and FeO of Earth mantle (McDonough & Sun 1995) and of Martian mantle (Yoshizaki & McDonough 2020) are shown for reference.

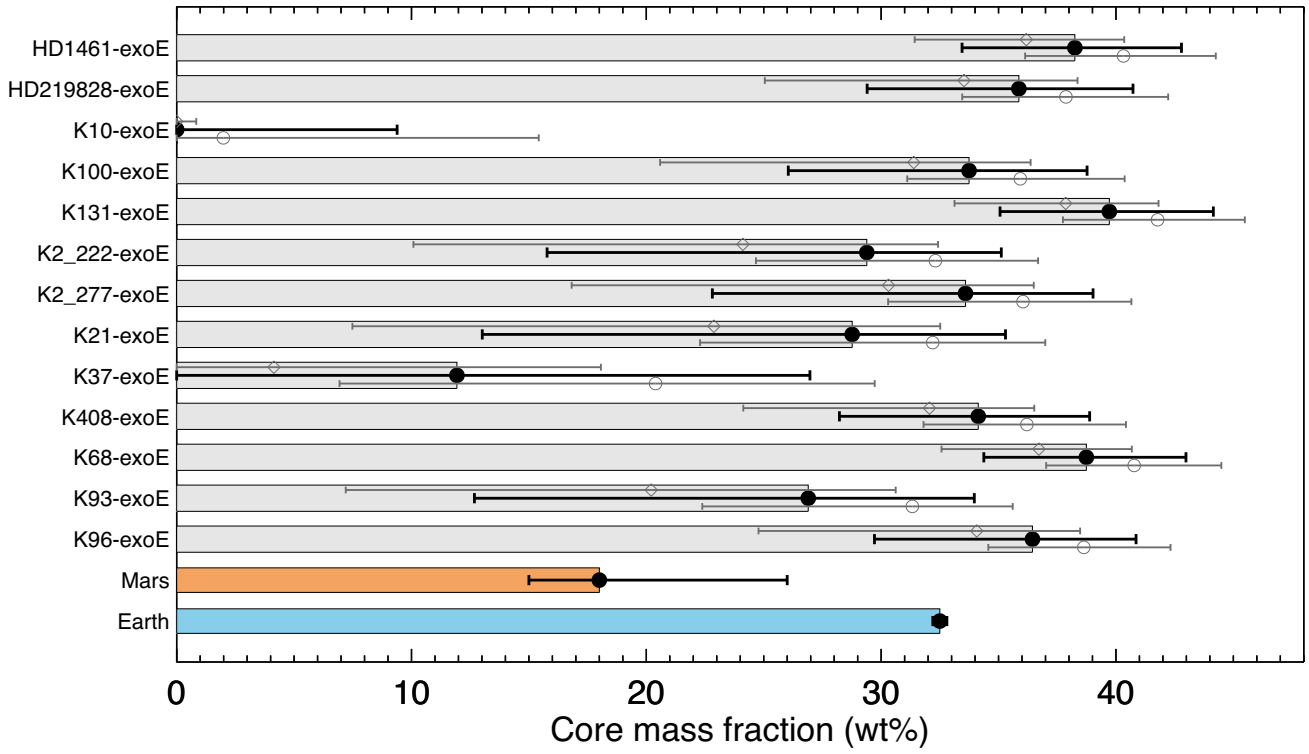

Figure 4. Estimates of the CMFs of the sample of model exo-Earths under three different scenarios: (i) applying the standard Sun-to-Earth devolatilization pattern (i.e. with the 1σ-uncertainty range) of W19a (filled circles with error bars in black); (ii) applying the 3σ upper limit of the standard devolatilization model (open diamonds with error bars in grey); (iii) applying the 3σ lower limit of the standard devolatilization model (open circles with error bars in grey). Earth's CMF (32.5 $\pm$ 0.3 wt per cent; Wang et al. 2018) and Mars' CMF (18^{+8}_{-3} wt per cent; Yoshizaki & McDonough 2020) are shown for reference.

is essential to correctly distribute oxygen into those more abundant oxides.

3.3 Mineralogy and internal structure

Using Kepler-21 exo-Earth (K21-exoE) as an example, we present its best-fitting mineralogy and structure (in terms of self-consistent

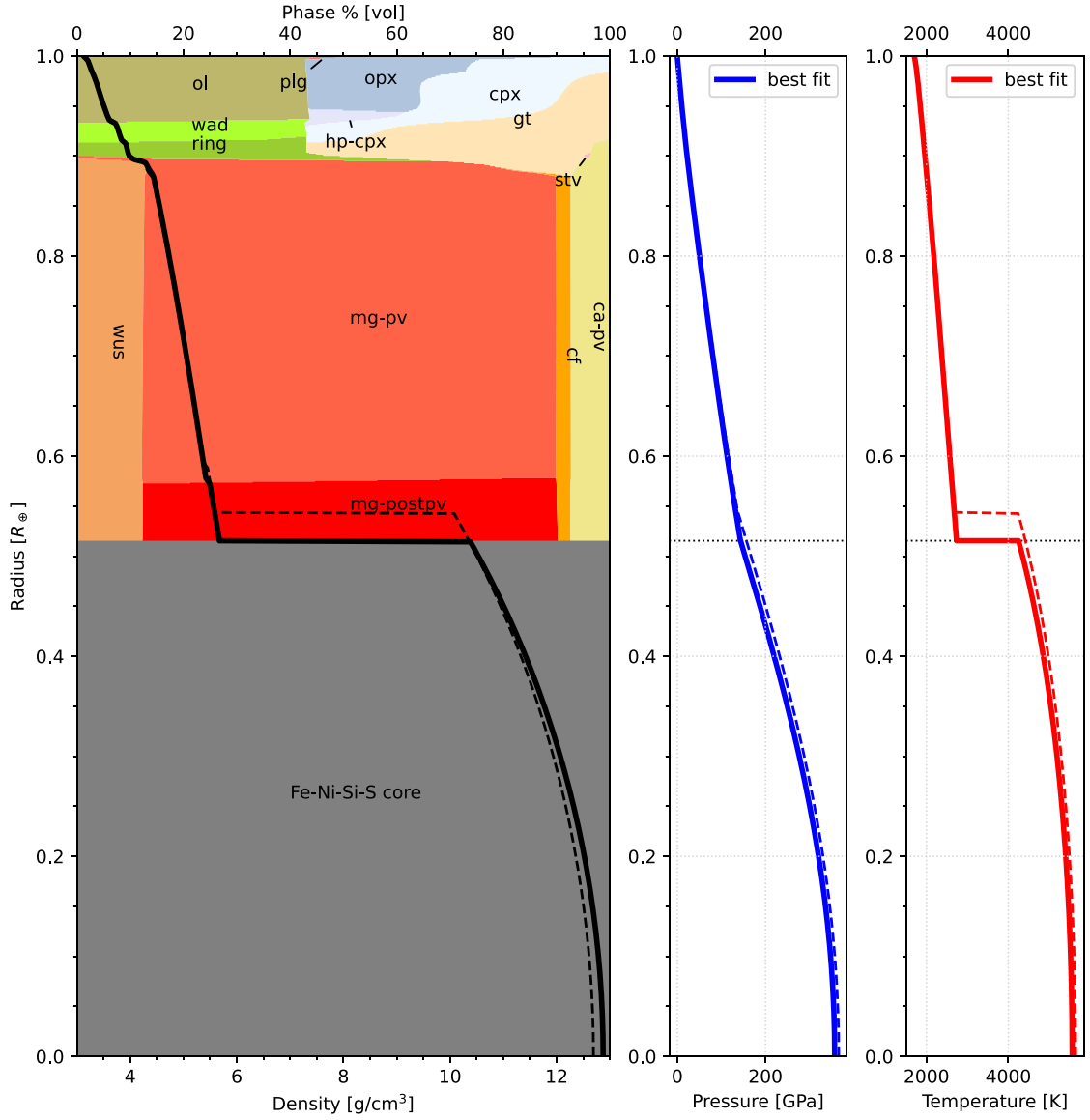

Figure 5. The best-fitting interior mineralogy and structure of Kepler-21 exo-Earth (as an example). The solid black, blue, and red curves are, respectively, the density, pressure, and temperature profiles of the planet. For reference, the corresponding profiles of the Earth are shown as dashed curves. The grey regime on the left-hand panel represents the core, which is presumably composed of Fe, Ni, Si, and S (the sum of which is normalized to 1). The temperature jumps at the CMBs are introduced by following Noack & Lasbleis (2020), resulting in 1513 K for K21-exoE and 1537 K for Earth. The abbreviations for mantle mineralogy stand for: ol - olivine, plg - plagioclase, opx - orthopyroxene, cpx - clinopyroxene, hp-cpx - high-pressure clinopyroxene, wad - wadsleyite, ring - ringwoodite, gt - garnet, stv - stishovite, wus - magnesiowüstite (ferropericlase), mg-pv - magnesium perovskite (bridgmanite), mg-postpv - magnesium postperovskite, cf - calcium-ferrite structured phase, and ca-pv - calcium perovskite. For other details of the model see text.

pressure, temperature and density profiles) in Fig. 5. It shows that in the upper mantle, pyroxenes (orthopyroxene – 'opx', clinopyroxene – 'cpx', and high-pressure clinopyroxene – 'hp-cpx') are relatively enriched over olivine ('ol'), being consistent with the planet's relatively low Mg/Si ratio (the left-hand panel of Fig. 2). The lower mantle (starting from the density jump at $\sim 0.9\ R_\oplus$) is dominated by magnesium (post-)perovskite ('mg-pv' and 'mg-postpv') and is similar to the Earth's lower mantle composition (Palme & O'Neill 2014). By comparing its density profile with the Earth's [in both cases a (plausible) inner solid core has been ignored; Fig. 5], K21-exoE has a best-fitting core slightly smaller than that of Earth. Please note that the best-fitting result is obtained at the mean values of the first-order major oxides and CMF (Table B1) and at a radius of 1 $R_\oplus$ (with its self-consistent mass, returned together with the mineralogy, equivalent to 1 $M_\oplus$ as well). The uncertainties of the best-fitting results for each mineral in the mantle and the radius fraction of the core, as well as other structural profiles (Fig. B3) are obtained at the 16 per cent and 84 per cent quartiles of a population of the mineralogy and structure analyses repeated from a random draw of the estimates of the mantle and core compositions, as well as CMFs (Table B1).

The best-fitting results for all planets, as shown in Figs B4 and B5, reveal that most of these exo-Earths are generally Earth-like in both mineralogy and structure. The notable exceptions are K10-exoE and K37-exoE. The former has a negligible core – as shown in Fig. 4 as well – and a gigantic mantle, whereas the latter has a core that is comparably smaller than all cases other than K10-exoE.

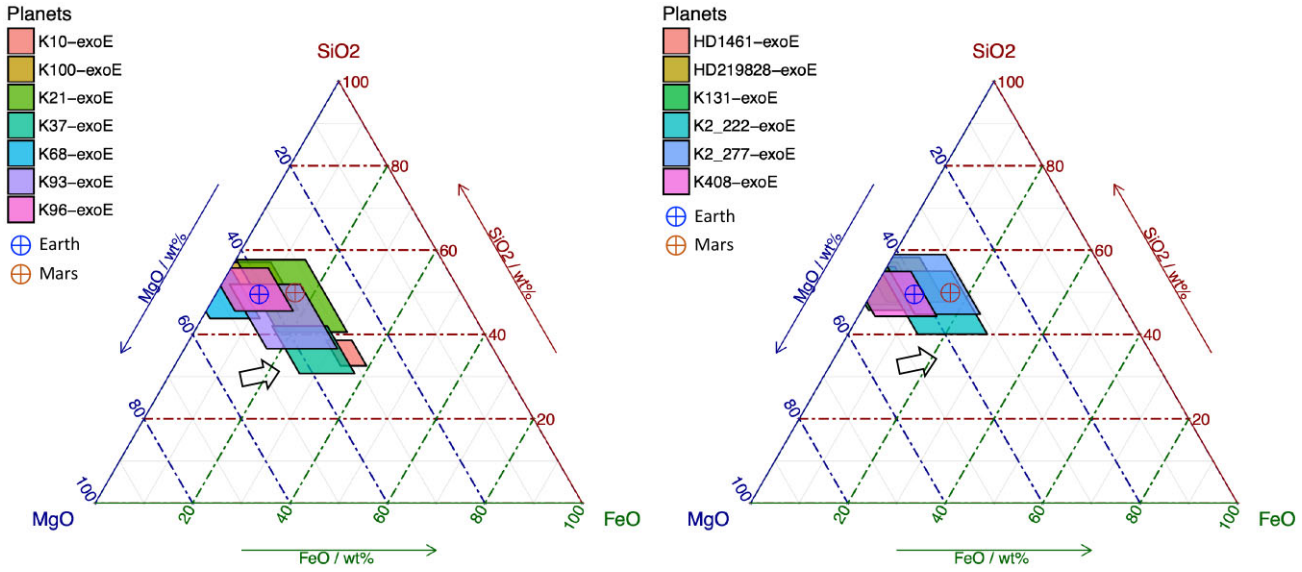

Figure 6. Similar to Fig. 3, but constrained with the 3σ upper limit of the Sun-to-Earth devolatilization pattern (W19a). The open arrow indicates the overall direction that the mantle composition shifts towards the parameter space of the ternary diagram. For details see Section 4.1.

Further, both have a deep mantle dominated by the high-pressure, 'mg-postpv' phase – compared to the 'mg-pv' phase (bridgemanite) for other cases. For the uppermost mantle (above ∼0.95 $R_{\oplus}$), it is dominated by olivine over pyroxene assemblages (also similar to that of Earth; Palme & O'Neill 2014) for all exo-Earth cases, except K2-277-exoE (and to a lesser degree, K21-exoE as well). Particularly, K2-277-exoE is also the only planet with a mean value of Mg/Si < 1 (Fig. 2). This highlights the significance of Mg/Si in determining the mantle mineralogy, as investigated in Hinkel & Unterborn (2018) and Spaargaren et al. (2020) as well. The intermediate range between upper and lower mantle (∼0.9-0.95 $R_{\oplus}$; i.e. the mantle transition zone) is dominated by wadsleyite ('wad') and ringwoodite ('ring') (also similar to Earth's scenario), except for K10-exoE, K37-exoE, K68-exoE, and K2-277-exoE. Considering that both wadsleyite and ringwoodite can store water in their crystal structures by about one order of magnitude higher than any other minerals, including olivine, pyroxene, and perovskite (Bercovici & Karato 2003; Pearson et al. 2014; Fei et al. 2017), these exceptional planets may also be the ones among the sample with the least interior water-storage capacity, although this assessment needs to be treated with caution considering the yet-large uncertainty in the modelled mantle mineralogy.

Broadly speaking and by considering the uncertainty level of such an analysis (as assessed for K21-exoE as an example), all of these cases (except K10-exoE and K37-exoE) share *both* the internal structure *and* mineralogy of a broadly Earth-like planet.

4 DISCUSSION

4.1 The effect of varying devolatilization scales on the interiors

Planet formation is a complex process. A variety of outcomes for the bulk composition of a rocky planet may result from composition-, location-, and time-scale-dependent differences in various devolatilization processes (W19b; Dorn et al. 2019; Harrison et al. 2021). Our empirical understanding of the devolatilization from the protosolar to terrestrial abundances cannot be a true reflection of the devolatilization that occurred in another planetary system, even for 'exo-Earths' by our definition. However, we suppose that the discrepancy is not dramatic concerning the similar Earth-like composition for rocky exoplanets as revealed by the abundance measurements on polluted white dwarfs (Doyle et al. 2019).

To explore the effect of varying the devolatilization scales on the interiors of exo-Earths, we apply the upper and lower limits of the 3σ range of the adopted devolatilization model to the abundances of these host stars. As a result, we obtain two alternative sets of planetary bulk compositions, corresponding to the 'less-depleted' (Fig. 6) and 'more-depleted' (Fig. 7) scenarios, respectively. In the 'less-depleted' scenario (Fig. 6), the mantle compositions (normalized by MgO + SiO_2 + FeO = 100 wt per cent) of these exo-Earths shift towards the direction where SiO_2 and FeO are more enriched (relative to the scenario under the standard devolatilization model – Fig. 3). In such a case, oxygen – acting as a critical element to the mantle composition estimate – is much less depleted, resulting in a much higher mantle oxidation state and thus more Si and Fe in the planet being oxidized. Likewise, in the 'more-depleted' scenario (Fig. 7), the normalized mantle compositions shift towards the direction where SiO_2 and FeO are more depleted (relative to the scenario under the standard devolatilization model – Fig. 3). In this case, oxygen is much more depleted, resulting in a reduced mantle and an increased amount of Si as well as Fe partitioned into the core.

The effect of such varied devolatilization scales is also reflected on to the modelled CMFs (Fig. 4). In the 'less-depleted' scenario (shown as open diamonds withe error bars in Fig. 4), the CMFs are systematically smaller than those under the 'standard' scenario (i.e. filled circles with error bars in Fig. 4), because the mantle is more oxidized with a reduced fractionation of metallic Fe and its alloy elements (Ni, Si, and S) into the core. Similarly, in the 'more-depleted' scenario (shown as open circles with error bars in Fig. 4), the CMFs are systematically larger than those under the 'standard' scenario. In such a case, the mantle is more reduced and a larger fraction of Fe and its alloy elements is partitioned into the core. It is also noteworthy that the limits of our calculated CMFs (0–46 per cent) under the different scenarios are statistically broader than those constrained by the uncorrected stellar compositions in the literature – e.g. 20–46 per cent (Plotnykov & Valencia 2020) and 21–41 per cent (Schulze et al. 2021) – and narrower than those

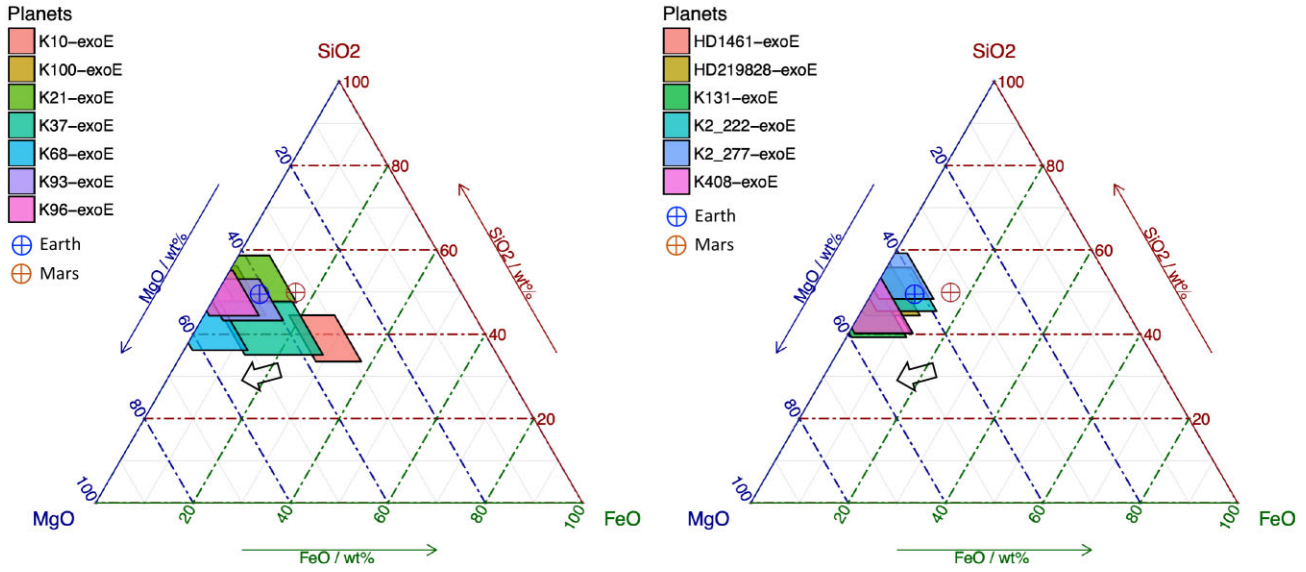

Figure 7. Similar to Fig. 3, but constrained with the 3σ lower limit of the Sun-to-Earth devolatilization pattern (W19a). The open arrow indicates the overall direction that the mantle composition shifts towards the parameter space of the ternary diagram. For details see Section 4.1.

constrained purely by mass and radius measurements – e.g. 1–92 per cent (Plotnykov & Valencia 2020) and 0–73 per cent (Schulze et al. 2021) for (potentially) rocky planets. These discrepancies are fundamentally attributed to (i) the difference in the available oxygen budget relative to other rock-forming elements in a planet (W19b) and (ii) the inherent degeneracy in constraining planetary interiors with only mass and radius measurements (Dorn et al. 2015). For a detailed discussion of model and observational uncertainties on the determination of planetary interiors, we refer the reader to Otegi et al. (2020).

Such a variance in the devolatilization scales also induces a change to the modelled internal structure and mineralogy (Fig. 8; K21-exoE is taken for example, in comparison with Fig. 5). In the 'less-depleted' scenario (left-hand panel), the modelled core-mantle boundary (in line with the horizontal part of the solid black curve) is relatively deeper than that modelled under the 'standard' scenario (dashed black curve), while it is opposite in the 'more-depleted' scenario. For the mantle mineralogies as modelled under various scenarios, there are no significant differences, except for the minerals (e.g. ringwoodite – 'ring', wadsleyite – 'wad', and stishovite – 'stv') in the mantle transition zone and the high-pressure 'mg-postpv' phase just above the core-mantle boundary. Overall, the variability of the devolatilization scaling factors seems to influence more the internal structure than the mantle mineralogy. As explained in Section 3.1, Mg/Si plays a critical role in modulating the mantle mineralogy, whereas this ratio is only *negligibly* altered by devolatilization (W19a). On the other hand, the fractionation of Fe between core and mantle is directly related to the mantle oxidation state (Righter 2003) and oxygen is a volatile (sensitive to devolatilization); consequently, the internal structure may be more affected when the devolatilization scale varies.

It is noteworthy that our exploration of the effect of varied devolatilization scales may not be applicable to peculiar planets such as super-Mercuries (e.g. Adibekyan et al. 2021), nor to any type of planets around M stars such as the TRAPPIST-1 system (Gillon et al. 2017) and Proxima b (Anglada-Escudé et al. 2016). This arises from potentially dramatic differences in planet formation histories and/or in stellar properties (e.g. XUV fluxes). To take into account these factors, a comprehensive investigation of nebular condensation (e.g. Wang, Sossi & Quanz 2020a), disc evolution (e.g. Bergner et al. 2020), hydrodynamic escape (e.g. Benedikt et al. 2020), accretionary dynamics (e.g. Emsenhuber et al. 2021), and impacts (Helffrich, Brasser & Shahar 2019) are warranted. Before such a comprehensive investigation sheds more light on devolatilization (in a quantitative manner), however, the inclusion of such an empirical model is a first-order but an integral part of the efforts in reducing the modelling degeneracies of interiors of terrestrial-type exoplanets.

4.2 The effect of varying mass and radius (within the terrestrial regime) on the interiors

As analysed in Section 3.3, these hypothetical exo-Earths are assumed to have a radius of 1 $R_\oplus$ and a mass of 1 $M_\oplus$. In reality, habitable-zone terrestrial planets are unlikely to be an ideal Earth 2.0 and their mass and radius may vary. To test the effect of varying mass and radius (within the terrestrial regime) on the interiors, we assume two extreme cases for the size of a model terrestrial planet by referring to the definition of a rocky planet orbiting within the (empirical) habitable zone: 0.5 and 1.5 $R_\oplus$ for the LIFE targets (Quanz et al. 2021). The mass is not predefined but computed together with the interiors by keeping the planet to be in the terrestrial regime. The modelling results are shown in Fig. 9.

For a model terrestrial planet of 0.5 $R_\oplus$ orbiting in the habitable zone of Kepler-21, its mantle mineralogy and self-consistent mass ($\sim$ 0.1 $M_\oplus$) approximately resemble those of Mars (Yoshizaki & McDonough 2020). For a model terrestrial planet of 1.5 $R_\oplus$ orbiting in the habitable zone of Kepler-21, however, there is no analogue in our Solar system, since its self-consistent mass of $\sim$ 4.3 $M_\oplus$ falls in the regime of a super-Earth and it has a lower mantle mineralogy distinctly dominated by the high-pressure 'mg-postpv' phase, while its upper mantle mineralogy resembles that of Earth (McDonough & Sun 1995; Palme & O'Neill 2014).

Please note that, both cases are conducted under the standard devolatilization model. Namely, the same set of the first-order mantle and core compositions, as well as CMF of Kepler-21 exo-Earth (Table B1) are input for producing Figs 5 and 9. In other words, the

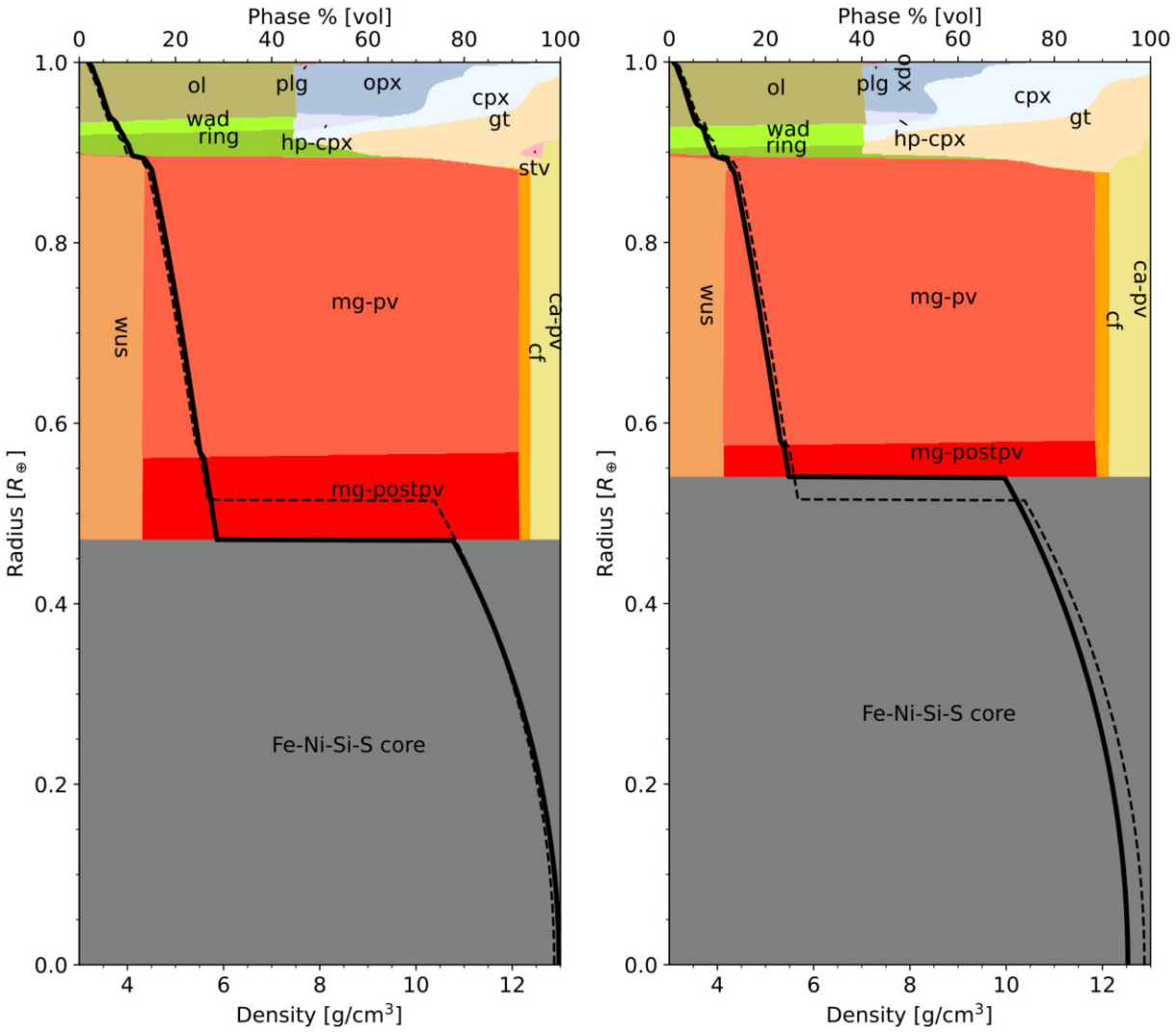

Figure 8. The modelled mineralogies and structures of Kepler-21 exo-Earth under two different devolatilization scenarios: the 3σ upper limit (left) and lower limit (right) of the Sun-to-Earth devolatilization pattern (W19a). For comparison, the density profile for the planet under the 'standard' scenario (Fig. 5) is replotted as a dashed curve in each panel.

significant differences in mantle mineralogy between these scenarios shown in Figs 5 and 9 are dictated only by the size (and implicitly the mass) of the model planet. The trivial differences in core radius fraction are related to the difference in density compression between the smaller and larger (model) planets.

4.3 On the precision requirement of using (devolatilized) host stellar abundances to constrain exoplanet interiors

In W19b, a precision level of $\lesssim$0.04 dex (differentially) or $\lesssim$10 per cent is proposed for the host stellar abundances to be used, upon devolatilization, to constrain and distinguish the interior compositions and structures of hypothetical terrestrial exoplanets. However, it is worth clarifying that this precision requirement does not take into account the uncertainty in the reference solar abundance, which is typically at the level of $\sim$0.03 dex (Asplund et al. 2009, 2021) for the aforementioned major rock-forming elements. If the latter were taken into account, the precision requirement for the host stellar abundances should be as small as $\sim$0.025 dex (differentially) or $\sim$6 per cent, which has been achieved with high-precision spectroscopic analysis for bright Sun-like stars (e.g. Paper I; Spina et al. 2021) and binary stars (Liu et al. 2018, 2021; Morel 2018). Apart from the concern with the precision, there are also non-trivial systematic differences between different reference solar abundances (e.g. Wang et al. 2019a; Lodders 2020; Adibekyan et al. 2021; Asplund et al. 2021). Therefore, one must clarify which solar abundances are applied for converting the stellar differential abundances to the absolute abundances, which are then used for further modelling of the properties of individual planets. For a detailed discussion of the systematic differences between stellar abundances determined with different techniques and their impacts on many aspects including modelling planetary properties, please refer to Hinkel et al. (2016).

4.4 Remaining limitations

For our interior structure model, we must emphasize that it is a rigid two-layer model – i.e. mantle + core, without the layers such as crust and water, nor that we have divided the core to an inner component and an outer one. Considering the currently typical uncertainties of

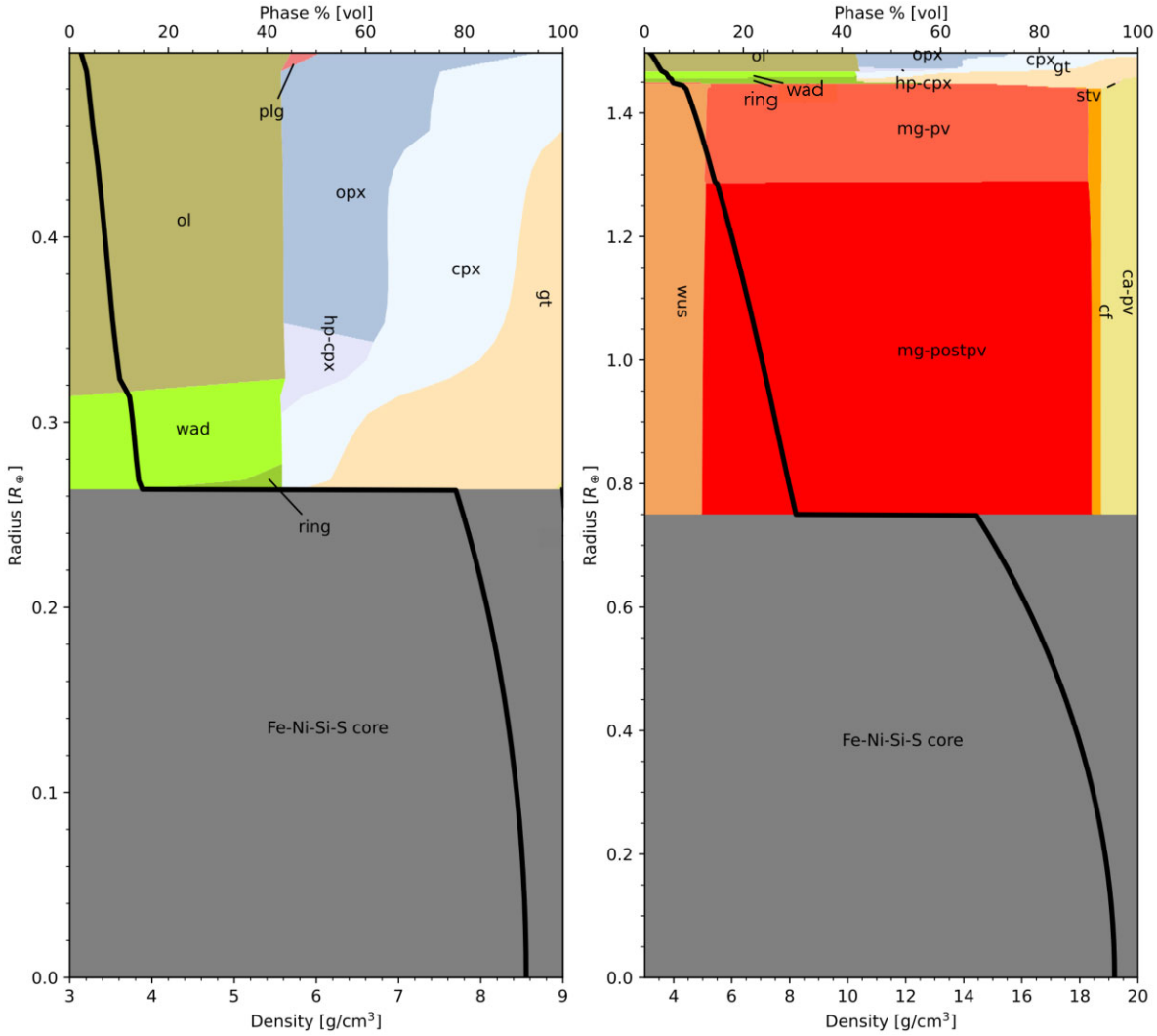

Figure 9. The modelled mineralogies and structures of Kepler-21 exo-Earth under the standard devolatilization scenario but with different assumptions of planetary size: $0.5R_\oplus$ (left) and $1.5R_\oplus$ (right). The returned, self-consistent masses are 0.1 and 4.3 $M_\oplus$, respectively, enabling the planet to be within the terrestrial regime. Please note that the CMB temperature jumps are introduced by following Stixrude (2014), instead of Noack & Lasbleis (2020) (which is parametrized for rocky planets of [0.8, 2] $M_\oplus$), for these two cases. Please also note the differences in the scales of radius and density between the two panels.

5–10 per cent and 10–20 per cent, respectively, for radius and mass measurements (Otegi et al. 2020), such a simplification is practical for interior modelling and has a trivial effect on our estimates of mantle composition and internal structure (in terms of core radius/mass fraction). The modelling of crust formation and composition is an active field and usually involves the modelling of partial melts, tectonics, and even weathering (Rozel et al. 2017; Brugman, Phillips & Till 2021; Hakim et al. 2021), which are however beyond the scope of this paper. None the less, our estimates of mantle mineralogy and core size provide essential information for future modelling of the crust owing to the fact that the crust is fundamentally an extraction product of the upper mantle through magmatic processes (Rozel et al. 2017; Noack, Breuer & Spohn 2012) and is also (ultimately) influenced by core formation (Dyck et al. 2021).

A water layer (while without a crust layer) has been considered in other interior models (e.g. Tian & Stanley 2013; Noack et al. 2016; Brugger et al. 2017; Dorn et al. 2017; Unterborn et al. 2018; Acuna et al. 2021). Based on numerical modelling, Shah et al. (2021) found that for a rocky planet with a mass of 0.1–3 $M_\oplus$, the effect of an isolated surface water (i.e. oceans) on the radius is $\leq$5 per cent, while the effect of a hydration case (i.e. water being chemically mixed with minerals) is $\leq$2.5 per cent – see also Vazan, Sari & Kessel (2022). Such effects are still within the currently typical uncertainty for radius but may become more profound with the continuous improvement of the precisions of mass and radius measurements (e.g. up to 5 per cent and 3 per cent, respectively; Stassun et al. 2017). The effect of water inclusion on the mass of a terrestrial-type planet should be nevertheless negligible. However, water (regardless of its amount) should be critically taken into account while extending a study on mineralogy and structure to that on internal dynamics (Evans et al. 2014; Spaargaren et al. 2020) and/or crust formation (Collins et al. 2020).

Finally, we treat the core to be completely molten and homogeneously composed of Fe, Ni, Si, and S, without differentiating a plausible inner solid portion made of pure Fe and Ni from an outer liquid portion that contains the light elements (McDonough 2003; Hirose et al. 2013; Wang et al. 2018). This may inevitably underestimate the core mass and thus overestimate core radius, in the

case that the core of the planet is differentiated. However, we envisage that the under-/over-estimation should not be significant, concerning that Earth's inner solid core just accounts for 5 per cent of the mass of the core (Yoder 1995; McDonough 2017) and that even a planet as small as Mars has been suggested to be in a molten state based on the most recent seismic data from the *InSight* mission (Stähler et al. 2021). Conflicting views on liquid/solid cores for super-Earths have been presented (e.g. Valencia, O'Connell & Sasselov 2006; Morard et al. 2011), so do the models underpinning the two scenarios – cf, 'solid' (Brugger et al. 2017; Dorn et al. 2017) versus 'liquid' (Lorenzo 2018; Unterborn et al. 2018). The phase of a planet's core should be not only related to the planet's mass and size but also its formation history and age (Stevenson 2008; Stixrude 2014). Before we know better about such information collectively, this issue will remain open for further discussion.

5 SUMMARY AND CONCLUSIONS

Based on the detailed chemical compositions of planet-hosting stars obtained in Paper I and Liu et al. (2016), this work extends the analysis of W19a,b and goes beyond the estimates of the first-order mantle oxide composition, core composition and CMF to the detailed mineralogy (i.e. complex mineral phases that are often seen in a rocky planet like Earth), and interior structure (in terms of not only CMF, but also core radius fraction and self-consistent density, pressure and temperature profiles). We have also assessed the uncertainties of the detailed interior estimates, which are contributed from the uncertainties associated with the host stellar abundances, the devolatilization pattern, as well as the interior modelling degeneracy. Further, by respectively varying the devolatilization scales and the planetary size, we test how such variabilities will affect the modelled interiors of terrestrial-type planets.

We find that among the 13 model exo-Earths, 11 are broadly Earth-like in both interior composition and structure, whereas Kepler-10 and Kepler-37 exo-Earths [both with high (O-Mg-2Si)/Fe, implying a high planetary oxidation state] are predicted to have substantially smaller cores. On the effect of varying devolatilization scaling factors on planetary interiors, we find that interior structure is more affected than mantle mineralogy, probably because the fractionation of Fe between mantle and core is more sensitive to the planetary oxidation state – thus determining the core size, whereas the mantle mineralogy is crucially modulated by Mg/Si (Hinkel & Unterborn 2018; Spaargaren et al. 2020) while this ratio is negligibly altered by devolatilization (W19a). The further test of varying the planetary size (and implicitly mass, by keeping within the terrestrial regime) reveals the potential diversity of the mantle mineralogy of terrestrial planets even if they might have experienced an equivalent devolatilization. We also recommend a precision level of $\lesssim$0.025 dex for the stellar differential abundances and a clarification of the reference solar abundances (and their uncertainties) in modelling planetary bulk composition and interiors.

Our model is unquestionably limited by its rigid assumption of a two-layer structure – i.e. mantle and core, with no crust (lithosphere) or water (potentially biosphere) considered yet, nor have we differentiated the core to be an inner component and an outer one based on their extent of solidification/crystallization. However, such a simplification should have little impact on our modelling results of the overall, mantle mineralogy and interior structure, while the model will be undoubtably refinable when the mass and radius measurements of real terrestrial planets become much more precise (e.g. up to 5 per cent and 3 per cent; Rauer et al. 2014; Stassun et al. 2017).

Exercised with caution, such a theoretical study (with a yet-large uncertainty) nevertheless offers an insight, based on the available data (essentially host stellar composition as well as planetary mass and radius), into the detailed properties of habitable-zone, terrestrial-type exoplanets. This provides guidance in the target selections for future missions, such as PLATO (Rauer et al. 2014; Nascimbeni et al. 2022), Ariel (Turrini et al. 2021), and LIFE (Quanz et al. 2021, 2022).

ACKNOWLEDGEMENTS

We thank the reviewers, particularly Lena Noack, for their helpful comments, which have greatly improved the quality of the manuscript. This work has been carried out within the framework of the National Centre of Competence in Research PlanetS supported by the Swiss National Science Foundation (SNSF). HSW and SPQ acknowledge the financial support of the SNSF. FL acknowledges the support of the Australian Research Council through Future Fellowship grant FT180100194. SJM thanks the Research Centre for Astronomy and Earth Sciences (Budapest, Hungary) and the Hungarian Academy of Sciences (MTA) for support. SJM extends special thanks to the University of Vienna, Department of Lithospheric Research (Vienna, Austria) for the Ida Pfeiffer Guest Professorship at which time a portion of the manuscript was completed.

DATA AVAILABILITY

The spectral data underlying this article are available in Keck Observatory Archive at https://koa.ipac.caltech.edu/cgi-bin/KOA/nph-KOAlogin. They can be accessed with Keck Program ID: Z148 (Semester: 2016B, PI: Yong) and Z279 (Semester: 2018A, PI: Yong). Other data underlying this article are available in the article or in the specified references.

REFERENCES

Acuna L., Deleuil M., Mousis O., Marcq E., Levesque M., Aguichine A., 2021, A&A, 647, 1
Adibekyan V. et al., 2021, Science (80-.)., 374, 330
Anderson D. L., 2000, Geophys. Res. Lett., 27, 3623
Anglada-Escudé G. et al., 2016, Nature, 536, 437
Asplund M., Grevesse N., Sauval A. J., Scott P., 2009, ARA&A, 47, 481
Asplund M., Amarsi A. M., Grevesse N., 2021, A&, 653, A141
Bedell M. et al., 2018, ApJ, 865, 68
Benedikt M. R., Scherf M., Lammer H., Marcq E., Odert P., Leitzinger M., Erkaev N. V., 2020, Icarus, 347, 113772
Bercovici D., Karato S. I., 2003, Nature, 425, 39
Bergner J. B. et al., 2020, ApJ, 898, 97
Bland P. a., Alard O., Benedix G. K., Kearsley A. T., Menzies O. N., Watt L. E., Rogers N. W., 2005, Proc. Natl. Acad. Sci. USA, 102, 13755
Bond J. C., O'Brien D. P., Lauretta D. S., 2010, ApJ, 715, 1050
Bonsor A., Jofré P., Shorttle O., Rogers L. K., Xu S., Melis C., 2021, MNRAS, 503, 1877
Bowens R. et al., 2021, A&A, 653, A8
Bower D. J., Kitzmann D., Wolf A. S., Sanan P., Dorn C., Oza A. V., 2019, A&A, 631, A103
Brewer J. M., Fischer D. A., 2016, ApJ, 831, 1
Brugger B., Mousis O., Deleuil M., Deschamps F., 2017, ApJ, 850, 93
Brugman K., Phillips M. G., Till C. B., 2021, J. Geophys. Res. Planets, 126, 1
Carlson R. W. et al., 2014, Annu. Rev. Earth Planet. Sci., 42, 151
Clark J. T. et al., 2021, MNRAS, 504, 4968
Collins W. J., Murphy J. B., Johnson T. E., Huang H. Q., 2020, Nat. Geosci., 13, 331

Connolly J. A. D., 2009, Geochem. Geophys. Geosyst., 10, Q10014
Cottrell E., Kelley K. A., 2011, Earth Planet. Sci. Lett., 305, 270
Davis A. M., 2006, in Lauretta D. S., McSween H. Y., eds, Meteorites Early Sol. Syst. II. University of Arizona Press, Tucson, Arizona, USA, p. 295
Delgado Mena E., Tsantaki M., Adibekyan V. Z., Sousa S. G., Santos N. C., González Hernández J. I., Israelian G., 2017, A&A, 606, A94
Dorn C., Khan A., Heng K., Connolly J. A. D., Alibert Y., Benz W., Tackley P., 2015, A&A., 577, A83
Dorn C., Venturini J., Khan A., Heng K., Alibert Y., Helled R., Rivoldini A., Benz W., 2017, A&A, 597, A37
Dorn C., Harrison J. H., Bonsor A., Hands T. O., 2019, MNRAS, 484, 712
Doyle A. E., Young E. D., Klein B., Zuckerman B., Schlichting H. E., 2019, Science, 366, 356
Dyck B., Wade J., Palin R., 2021, ApJ, 913, L10
Emsenhuber A., Mordasini C., Burn R., Alibert Y., Benz W., Asphaug E., 2021, A&A, 656, A69
Evans A. J., Zuber M. T., Weiss B. P., Tikoo S. M., 2014, J. Geophys. Res. E Planets, 119, 1061
Fei H., Yamazaki D., Sakurai M., Miyajima N., Ohfuji H., Katsura T., Yamamoto T., 2017, Sci. Adv., 3, 1
Frank E. a., Meyer B. S., Mojzsis S. J., 2014, Icarus, 243, 274
Gialluca M. T., Robinson T. D., Rugheimer S., Wunderlich F., 2021, PASP, 133, 054404
Gillon M. et al., 2017, Nature, 542, 456
Grossman L., Larimer J. W., 1974, Rev. Geophys., 12, 71
Hakim K., van Westrenen W., Dominik C., 2018, A&A, 618, L6
Hakim K., Spaargaren R., Grewal D. S., Rohrbach A., Berndt J., Dominik C., Van Westrenen W., 2019, Astrobiology, 19, 867
Hakim K. et al., 2021, Planet. Sci. J., 2, 49
Harrison J. H., Shorttle O., Bonsor A., 2021, Earth Planet. Sci. Lett., 554, 116694
Helffrich G., Brasser R., Shahar A., 2019, Prog. Earth Planet. Sci., 6, 66
Hinkel N. R., Unterborn C. T., 2018, ApJ, 853, 83
Hinkel N. R. et al., 2016, ApJS, 226, 4
Hirose K., Labrosse S., Hernlund J., 2013, Annu. Rev. Earth Planet. Sci., 41, 657
Kacar B., Garcia A. K., Anbar A. D., 2021, ChemBioChem, 22, 114
Kuwayama Y. et al., 2020, Phys. Rev. Lett., 124, 165701
Li J., Fei Y., 2014, in Carlson R. W., ed., Vol. 3, Treatise on Geochemistry, 2 edn., Elsevier, Amsterdam, Netherlands, p. 527
Liu F. et al., 2016, MNRAS, 456, 2636
Liu F., Yong D., Asplund M., Feltzing S., Mustill A. J., Meléndez J., Ramírez I., Lin J., 2018, A&A, 614, 1
Liu F., Yong D., Asplund M., Wang H. S., Spina L., Acuña L., Meléndez J., Ramírez I., 2020, MNRAS, 495, 3961 (Paper I)
Liu F., Bitsch B., Asplund M., Liu B.-b., Murphy M. T., Yong D., Ting Y.-s., Feltzing S., 2021, MNRAS, 508, 1227
Lodders K., 2003, ApJ, 591, 1220
Lodders K., 2020, in Read P., ed., Oxford Res. Encycl. Planet. Sci. Oxford Univ. Press, Oxford, UK, p. 17
Lorenzo A. J., 2018, Master's thesis, Arizona State University
McDonough W., 2003, in Carlson R. W., ed., Vol. 2, Treatise on Geochemistry, 1 edn., Elsevier, Amsterdam, Netherlands, p. 547
McDonough W. F., 2017, in White W., ed., Encycl. Geochemistry. Springer International Publishing AG, Basel, Switzerland, p. 418
McDonough W., Sun S.-s., 1995, Chem. Geol., 120, 223
Morard G., Bouchet J., Valencia D., Mazevet S., Guyot F., 2011, High Energy Density Phys., 7, 141
Morel T., 2018, A&A, 615, A172
Morley C. V., Kreidberg L., Rustamkulov Z., Robinson T., Fortney J. J., 2017, ApJ, 850, 121
Nascimbeni V. et al., 2022, A&A, 658, A31
Nissen P. E., 2015, A&A, 579, 1
Noack L., Lasbleis M., 2020, A&A, 638, A129
Noack L., Breuer D., Spohn T., 2012, Icarus, 217, 484
Noack L. et al., 2016, Icarus, 277, 215
O'Neill H., 1987, Am. Mineral., 72, 67
Ortenzi G. et al., 2020, Sci. Rep., 10, 1
Otegi J. F., Bouchy F., Helled R., 2020, A&A, 634, A43
Palme H., O'Neill H., 2014, in Carlson R. W., ed., Vol. 3, Treatise on Geochemistry, 2 edn., Elsevier, Amsterdam, Netherlands, p. 1
Pearson D. G. et al., 2014, Nature, 507, 221
Plotnykov M., Valencia D., 2020, MNRAS, 499, 932
Quanz S. P., Crossfield I., Meyer M. R., Schmalzl E., Held J., 2015, Int. J. Astrobiol., 14, 279
Quanz S. P. et al., 2021, Exp. Astron.
Quanz S. P. et al., 2022, A&A, in press
Rauer H. et al., 2014, Exp. Astron., 38, 249
Righter K., 2003, Annu. Rev. Earth Planet. Sci., 31, 135
Rozel A. B., Golabek G. J., Jain C., Tackley P. J., Gerya T., 2017, Nature, 545, 332
Santos N. C. et al., 2015, A&A, 580, L13
Schulze J. G., Wang J., Johnson J. A., Gaudi B. S., Unterborn C. T., Panero W. R., 2021, Planet. Sci. J., 2, 113
Shah O., Alibert Y., Helled R., Mezger K., 2021, A&A, 646, A162
Shahar A., Driscoll P., Weinberger A., Cody G., 2019, Science, 364, 433
Sossi P. A., Fegley B., 2018, Rev. Mineral. Geochem., 84, 393
Spaargaren R. J., Ballmer M. D., Bower D. J., Dorn C., Tackley P. J., 2020, A&A, 643, 1
Spaargaren R., Wang H., Ballmer M., Mojzsis S., Tackley P., 2021, in EGU Gen. Assem. 2021. online. Vienna, Austria, p. EGU21
Spina L., Sharma P., Meléndez J., Bedell M., Casey A. R., Carlos M., Franciosini E., Vallenari A., 2021, Nat. Astron., 11, 1163
Stähler S. C. et al., 2021, Science, 373, 443
Stassun K. G., Collins K. A., Gaudi B. S., 2017, AJ, 153, 136
Stassun K. G., Corsaro E., Pepper J. A., Gaudi B. S., 2018, AJ, 155, 22
Stevenson D. J., 2008, Nature, 451, 261
Stixrude L., 2014, Philos. Trans. R. Soc. A, 372, 20130076
Stixrude L., Lithgow-Bertelloni C., 2011, Geophys. J. Int., 184, 1180
Suárez-Andrés L., Israelian G., González Hernández J. I., Adibekyan V. Z., Delgado Mena E., Santos N. C., Sousa S. G., 2018, A&A, 614, A84
Teske J. K., Cunha K., Smith V. V., Schuler S. C., Griffith C. a., 2014, ApJ, 788, 39
Tian B. Y., Stanley S., 2013, ApJ, 768, 156
Tinetti G. et al., 2018, Exp. Astron., 46, 135
Turrini D. et al., 2021, Exp. Astron.
Unterborn C. T., Dismukes E. E., Panero W. R., 2016, ApJ, 819, 32
Unterborn C. T., Desch S. J., Hinkel N. R., Lorenzo A., 2018, Nat. Astron., 2, 297
Valencia D., O'Connell R. J., Sasselov D., 2006, Icarus, 181, 545
Vazan A., Sari R., Kessel R., 2022, ApJ, 926, 150
Wang H., 2018, PhD thesis, Australian National University
Wang H. S., 2022, in EGU Gen. Assem. 2022. EGU, Vienna, Austria, id. EGU22–10146, 23-27 May 2022
Wang H. S., Lineweaver C. H., Ireland T. R., 2018, Icarus, 299, 460
Wang H. S., Lineweaver C. H., Ireland T. R., 2019a, Icarus, 328, 287
Wang H. S., Liu F., Ireland T. R., Brasser R., Yong D., Lineweaver C. H., 2019b, MNRAS, 482, 2222
Wang H. S., Sossi P. A., Quanz S. P., 2020a, in Eur. Sci. Congr. 2020., online. id. EPSC2020–874
Wang H. S., Morel T., Quanz S. P., Mojzsis S. J., 2020b, A&A, 644, A19
Wang H. S., Lineweaver C. H., Quanz S. P., Mojzsis S. J., Ireland T. R., Sossi P. A., Seidler F., Morel T., 2022, ApJ, 927, 134
Weiss L. M. et al., 2016, ApJ, 819, 83
Yoder C., 1995, in Ahrens T., ed., AGU Ref. Shelf. 1: Global Earth Physics: A Handbook of Physical Constants. American Geophysical Union (AGU), Washington, D.C., USA, p. 1
Yoshizaki T., McDonough W. F., 2020, Geochim. Cosmochim. Acta, 273, 137

APPENDIX A: MODEL PLANETARY BULK COMPOSITIONS

Table A1. Model bulk compositions (normalized to Al=100) of hypothetical habitable-zone terrestrial exoplanets ('exoE'), as devolatilized[a] from their host stellar abundances[b]. The reported uncertainties are 1σ[c].

	C	O	S	Na	Si	Mg	Fe	Ni	Ca	Al
K10-exoE	41^{+10}_{-8}	3871^{+445}_{-403}	31^{+4}_{-4}	12^{+1}_{-1}	819^{+67}_{-62}	1048^{+92}_{-84}	679^{+72}_{-65}	38^{+4}_{-4}	66^{+5}_{-5}	100^{+7}_{-7}
K21-exoE	57^{+15}_{-12}	4862^{+642}_{-574}	46^{+6}_{-5}	23^{+3}_{-3}	1490^{+128}_{-117}	1515^{+135}_{-124}	1225^{+138}_{-124}	66^{+8}_{-7}	110^{+9}_{-8}	100^{+7}_{-7}
K37-exoE	30^{+7}_{-6}	2936^{+339}_{-307}	-	10^{+1}_{-1}	670^{+56}_{-51}	1013^{+85}_{-78}	617^{+65}_{-59}	34^{+4}_{-3}	59^{+5}_{-4}	100^{+28}_{-22}
K68-exoE	22^{+5}_{-4}	1857^{+213}_{-193}	20^{+2}_{-2}	10^{+1}_{-1}	649^{+53}_{-49}	744^{+61}_{-56}	597^{+63}_{-57}	35^{+4}_{-3}	51^{+4}_{-3}	100^{+35}_{-26}
K93-exoE	30^{+8}_{-7}	2889^{+332}_{-301}	28^{+3}_{-3}	12^{+1}_{-1}	776^{+64}_{-59}	996^{+83}_{-76}	716^{+75}_{-68}	41^{+4}_{-4}	65^{+6}_{-5}	100^{+12}_{-11}
K96-exoE	36^{+9}_{-7}	3176^{+361}_{-327}	34^{+4}_{-4}	14^{+1}_{-1}	1000^{+81}_{-75}	1152^{+95}_{-87}	1026^{+107}_{-97}	54^{+6}_{-5}	86^{+6}_{-6}	100^{+10}_{-9}
K100-exoE	42^{+10}_{-9}	2785^{+361}_{-323}	35^{+4}_{-4}	16^{+2}_{-1}	906^{+80}_{-73}	985^{+86}_{-79}	759^{+84}_{-76}	46^{+5}_{-5}	64^{+5}_{-5}	100^{+10}_{-9}
K131-exoE	32^{+9}_{-8}	2459^{+291}_{-263}	28^{+3}_{-3}	13^{+1}_{-1}	861^{+71}_{-65}	963^{+82}_{-75}	847^{+91}_{-82}	49^{+5}_{-5}	71^{+6}_{-5}	100^{+8}_{-7}
K2-222-exoE	54^{+22}_{-17}	3809^{+471}_{-424}	40^{+5}_{-5}	18^{+2}_{-2}	1125^{+96}_{-88}	1293^{+114}_{-104}	960^{+106}_{-96}	51^{+6}_{-5}	84^{+7}_{-6}	100^{+12}_{-11}
K2-277-exoE	44^{+13}_{-11}	3012^{+394}_{-353}	37^{+5}_{-4}	14^{+2}_{-1}	966^{+86}_{-78}	958^{+87}_{-79}	851^{+96}_{-86}	51^{+6}_{-5}	70^{+7}_{-6}	100^{+8}_{-7}
K408-exoE	44^{+11}_{-9}	3418^{+434}_{-390}	38^{+5}_{-4}	15^{+2}_{-2}	1125^{+101}_{-92}	1332^{+116}_{-107}	957^{+105}_{-95}	50^{+6}_{-5}	93^{+8}_{-7}	100^{+9}_{-8}
HD1461-exoE	36^{+9}_{-8}	2426^{+293}_{-264}	30^{+4}_{-3}	17^{+2}_{-2}	867^{+72}_{-66}	928^{+78}_{-72}	762^{+82}_{-74}	49^{+5}_{-5}	59^{+5}_{-4}	100^{+10}_{-9}
HD219828-exoE	33^{+9}_{-7}	2482^{+318}_{-286}	28^{+3}_{-3}	16^{+2}_{-1}	840^{+71}_{-65}	868^{+77}_{-70}	730^{+81}_{-73}	44^{+5}_{-4}	60^{+5}_{-5}	100^{+9}_{-9}

[a] The model of devolatilization: W19a – Wang et al. (2019a); the specific devolatilization factors for these listed elements can also be found in table 1 of W19b – Wang et al. (2019b).
[b] Sources of host stellar abundances: Paper I – Liu et al. (2020; table 2), except for Kepler 10 (Liu et al. 2016; table 2, derived with HET data)
[c] The uncertainties are propagated from the 1σ uncertainties in both host stellar abundances and in the devolatilization model.

APPENDIX B: MODELLING DETAILS OF PLANETARY INTERIORS

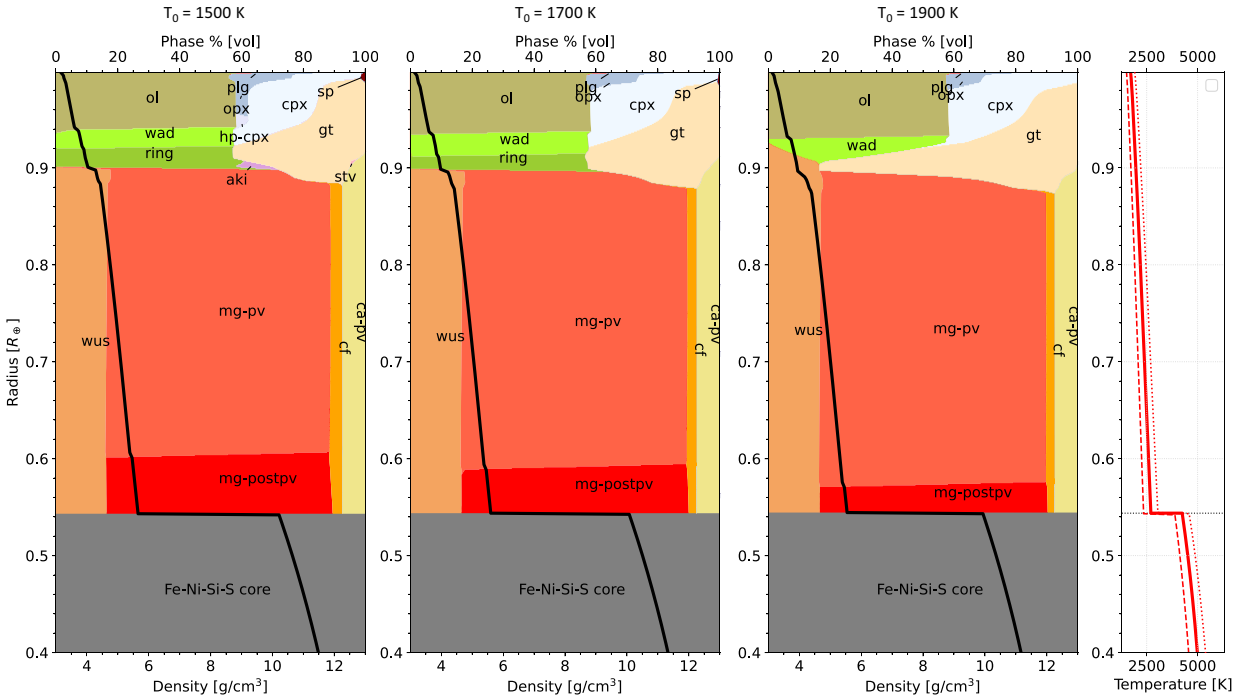

Figure B1. The comparison of the modelled mantle mineralogies in the case of Earth given different mantle potential temperatures (T_0): 1500, 1700, and 1900 K, which respectively correspond to the dashed, solid, and dotted curves in the right-most panel for the temperature profiles. The core-mantle temperature jump is fixed at 1537 K for all cases. The core in each case is only partially shown to highlight the mantle mineralogy.

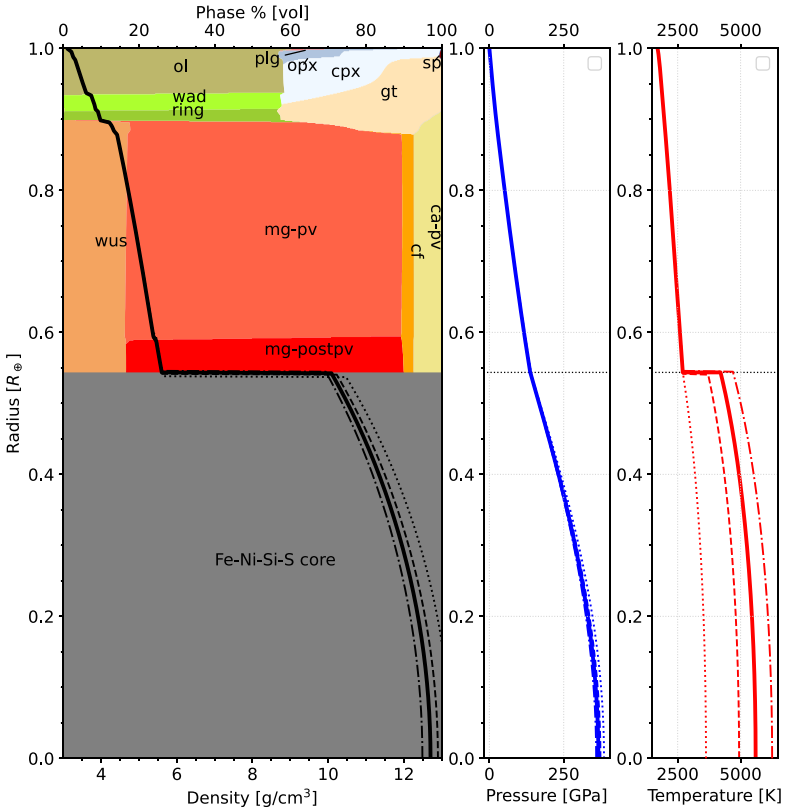

Figure B2. The comparison of the modelled interior profiles for density (black curves), pressure (blue curves), and temperature (red curves) in the case of Earth given different core-mantle temperature jumps: 0, 1000, 1500, and 2000 K, which respectively correspond to the dotted, dashed, solid, and dash–dotted curves of these profiles. The mantle potential temperature is fixed at 1700 K for all cases.

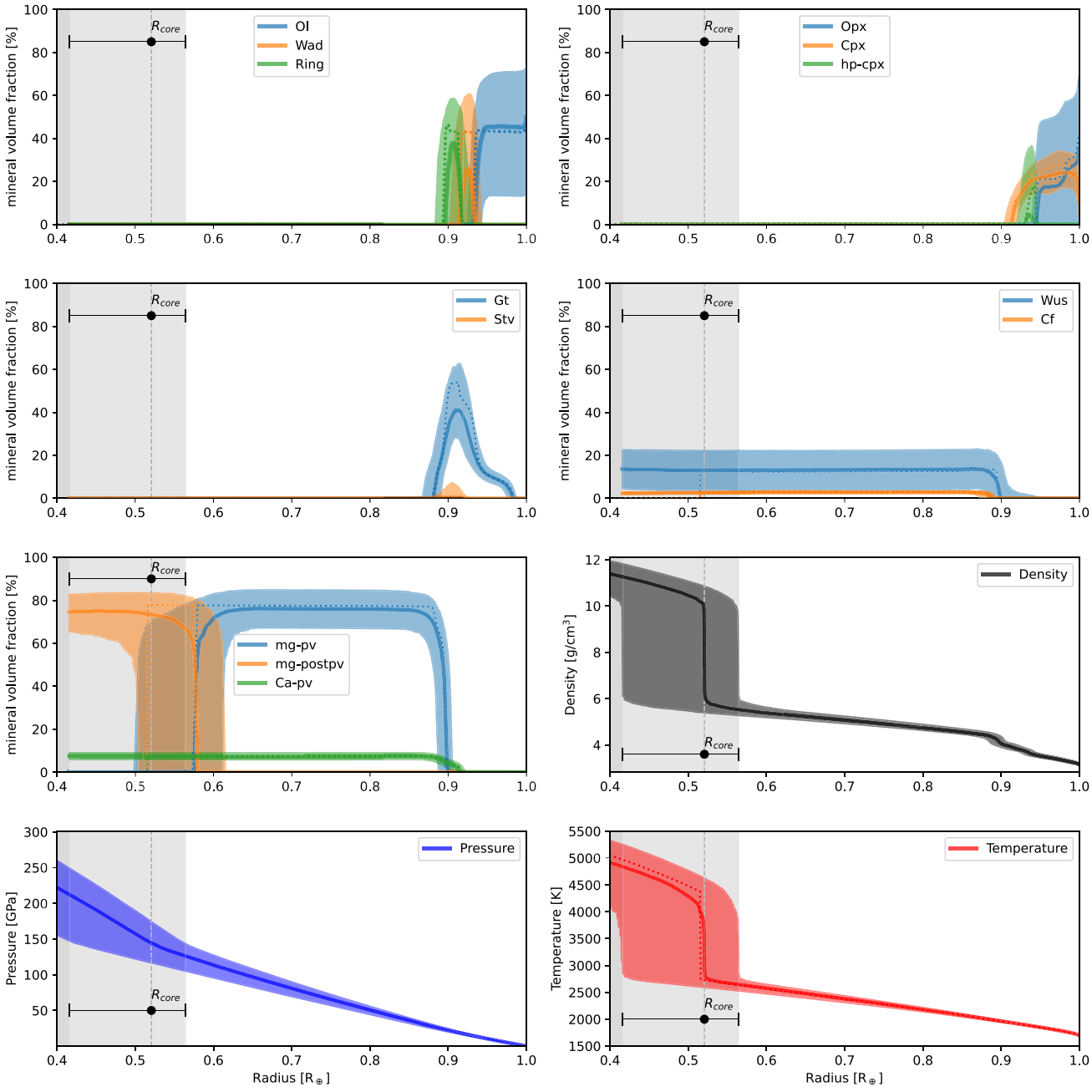

Figure B3. The uncertainty assessment of the modelled mineralogy and structure (taking K21-exoE as an example). The best-fitting mineralogy/structure profiles (corresponding to Fig. 5) are shown in dotted lines in each panel, with the 50th percentile and the range of 16th and 84th percentiles of the estimates shown in a solid line and a shadow area. The best-fitting profiles of pressure and density are exactly coincident with their 50th percentiles. The vertical dashed line in each panel indicates the 50th percentile of the core size ($R_{\rm core}$), with its uncertainty shown in the light grey area. The illustration of the 50th percentile and the embraced range of [16th, 84th] percentiles of the lower mantle mineralogy has been cut off beyond the 1σ lower limit of the radius.

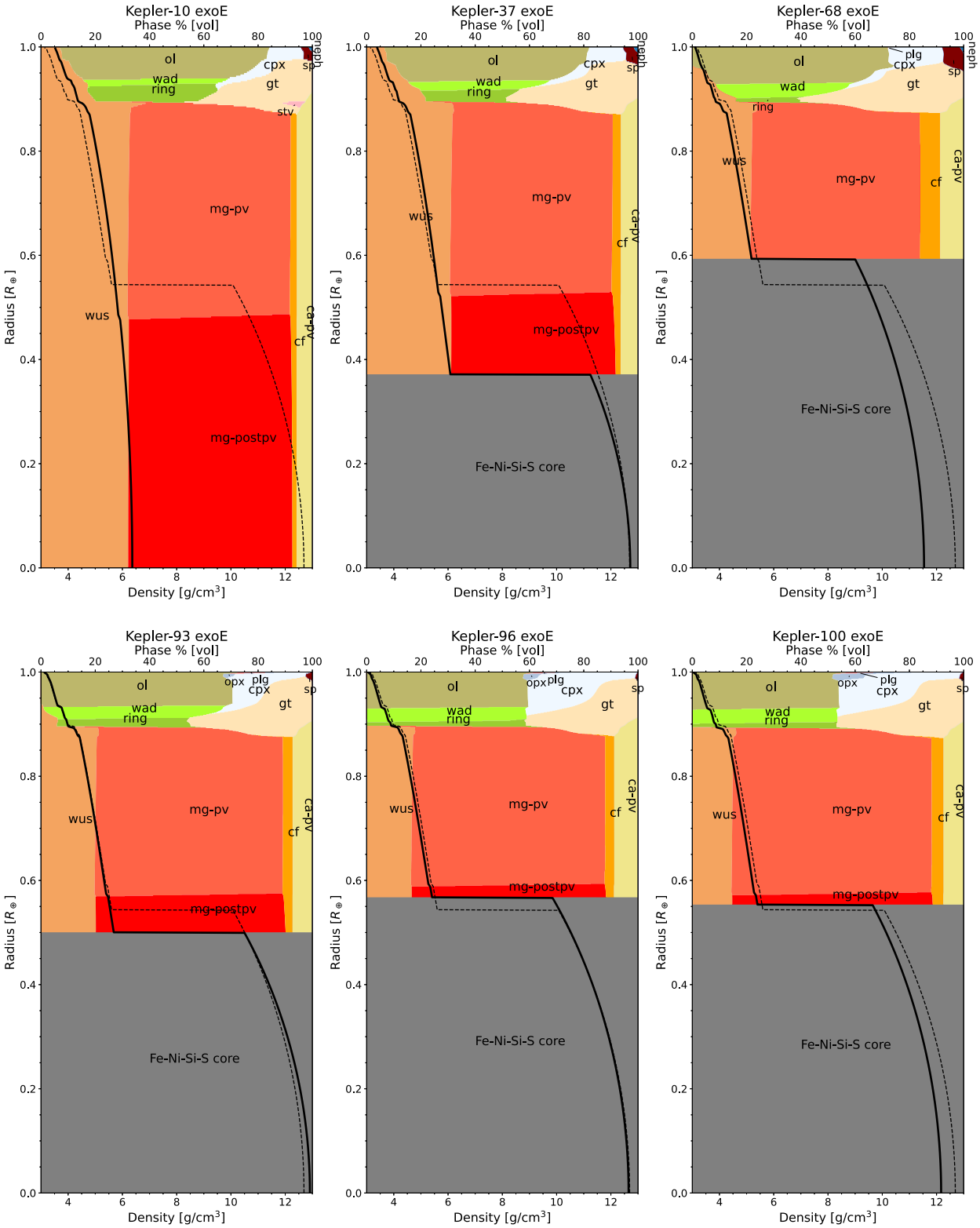

Figure B4. The best-fitting mineralogies and structures of half of the sample of exo-Earths. The dashed curves indicate the Earth density profile. For the explanation of other details of these individual diagrams, please refer to Fig. 5. The additional mineral name abbreviations – sp and neph – stand for spinel and nepheline, respectively.

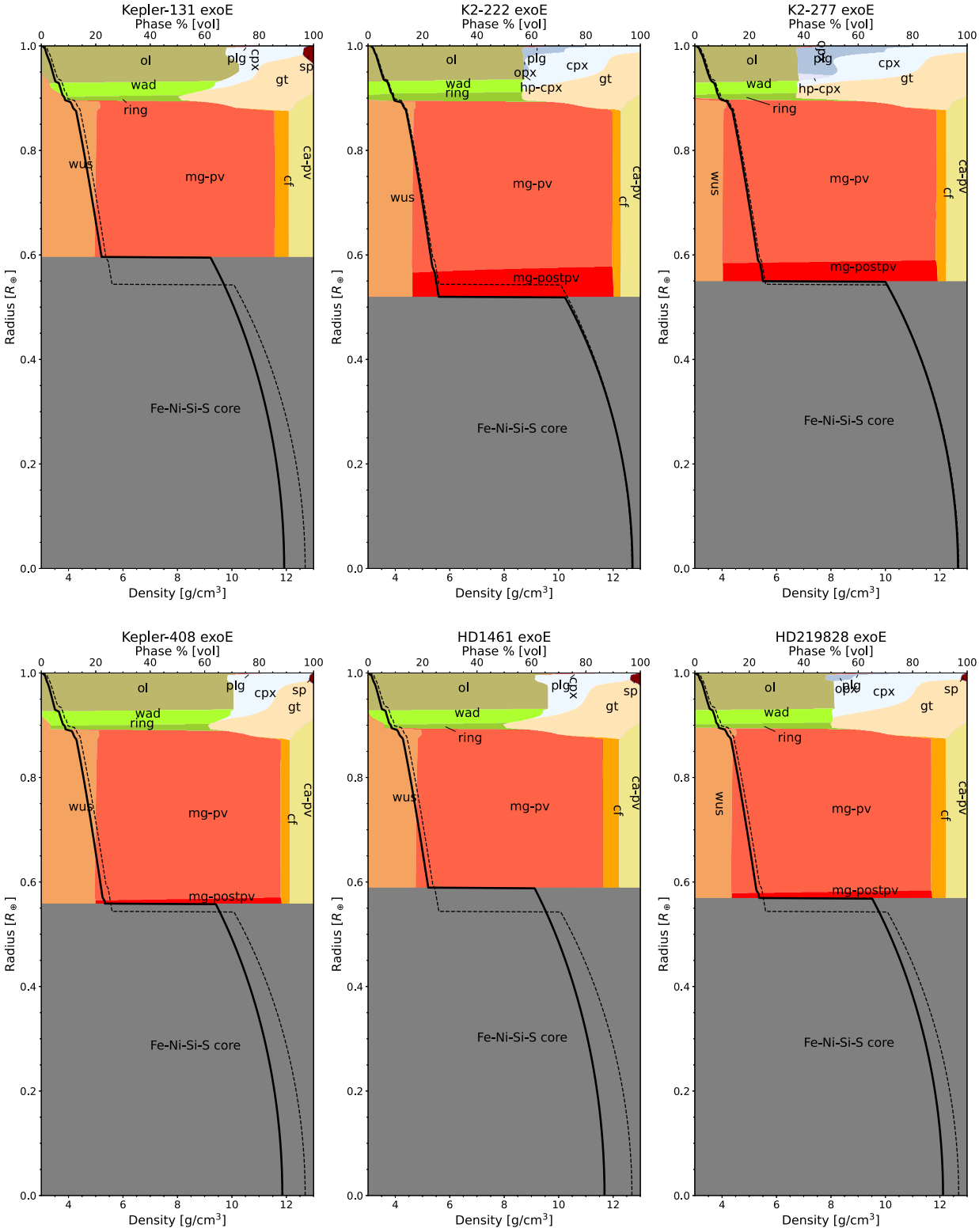

Figure B5. Similar to Fig. B4 but for the other half of the sample.

Table B1. Interior compositions and CMFs (with 1σ uncertainties) of hypothetical exo-Earths (exoE) around the sample of stars, in comparison with Earth.

	Mantle composition (wt per cent)										
	Na_2O	CaO	MgO	Al_2O_3	SiO_2	FeO	NiO	SO_3	CO_2	C	Metals
K10-exoE	$0.24^{+0.04}_{-0.03}$	$2.41^{+0.36}_{-0.24}$	$27.4^{+4.3}_{-2.6}$	$3.32^{+0.47}_{-0.30}$	$31.8^{+5.1}_{-2.9}$	$29.02^{+2.99}_{-5.32}$	$1.66^{+0.23}_{-0.38}$	$1.39^{+0.26}_{-0.42}$	$0.68^{+0.18}_{-0.17}$	$0.15^{+0.05}_{-0.05}$	-
K21-exoE	$0.41^{+0.09}_{-0.09}$	$3.52^{+0.62}_{-0.73}$	$35.2^{+6.2}_{-7.7}$	$2.92^{+0.51}_{-0.60}$	$47.8^{+5.3}_{-8.3}$	$8.62^{+6.89}_{-6.58}$	$0.42^{+0.47}_{-0.27}$	$0.50^{+0.10}_{-0.10}$	$0.03^{+0.01}_{-0.01}$	$0.38^{+0.12}_{-0.10}$	$0.15^{+0.28}_{-0.13}$
K37-exoE	$0.27^{+0.06}_{-0.04}$	$2.87^{+0.67}_{-0.45}$	$35.0^{+9.3}_{-5.5}$	$4.45^{+1.58}_{-1.15}$	$34.4^{+7.3}_{-5.5}$	$21.01^{+6.14}_{-11.56}$	$1.19^{+0.42}_{-0.75}$	-	$0.20^{+0.06}_{-0.07}$	$0.27^{+0.08}_{-0.07}$	$0.02^{+0.04}_{-0.02}$
K68-exoE	$0.49^{+0.07}_{-0.06}$	$4.32^{+0.55}_{-0.47}$	$45.6^{+5.6}_{-5.0}$	$7.82^{+2.73}_{-2.13}$	$41.0^{+5.7}_{-6.9}$	$0.22^{+0.43}_{-0.18}$	$0.03^{+0.02}_{-0.01}$	$0.04^{+0.01}_{-0.03}$	-	$0.41^{+0.10}_{-0.09}$	$0.03^{+0.15}_{-0.02}$
K93-exoE	$0.35^{+0.06}_{-0.07}$	$3.46^{+0.61}_{-0.66}$	$38.4^{+6.5}_{-7.7}$	$4.82^{+0.94}_{-0.96}$	$42.2^{+5.0}_{-7.2}$	$9.29^{+7.87}_{-7.10}$	$0.53^{+0.51}_{-0.33}$	$0.61^{+0.11}_{-0.12}$	$0.02^{+0.01}_{-0.01}$	$0.34^{+0.11}_{-0.09}$	$0.02^{+0.13}_{-0.02}$
K96-exoE	$0.38^{+0.05}_{-0.05}$	$4.31^{+0.56}_{-0.59}$	$41.5^{+5.3}_{-5.8}$	$4.53^{+0.68}_{-0.66}$	$45.7^{+4.2}_{-5.5}$	$2.47^{+2.90}_{-1.94}$	$0.12^{+0.16}_{-0.07}$	$0.25^{+0.05}_{-0.11}$	-	$0.38^{+0.10}_{-0.09}$	$0.37^{+0.52}_{-0.30}$
K100-exoE	$0.49^{+0.08}_{-0.08}$	$3.64^{+0.54}_{-0.57}$	$40.8^{+5.6}_{-6.2}$	$5.20^{+0.83}_{-0.83}$	$46.5^{+4.4}_{-6.1}$	$2.37^{+3.20}_{-1.89}$	$0.19^{+0.20}_{-0.10}$	$0.30^{+0.06}_{-0.13}$	-	$0.51^{+0.14}_{-0.12}$	$0.03^{+0.05}_{-0.02}$
K131-exoE	$0.47^{+0.07}_{-0.06}$	$4.56^{+0.59}_{-0.54}$	$44.7^{+5.5}_{-5.2}$	$5.85^{+0.77}_{-0.69}$	$43.5^{+5.2}_{-6.2}$	$0.39^{+0.61}_{-0.32}$	$0.04^{+0.04}_{-0.02}$	$0.07^{+0.02}_{-0.05}$	-	$0.43^{+0.14}_{-0.11}$	$0.05^{+0.37}_{-0.04}$
K2-222-exoE	$0.40^{+0.08}_{-0.08}$	$3.45^{+0.57}_{-0.65}$	$38.5^{+5.9}_{-7.7}$	$3.72^{+0.71}_{-0.73}$	$45.5^{+4.8}_{-7.1}$	$6.92^{+6.38}_{-5.37}$	$0.31^{+0.43}_{-0.19}$	$0.51^{+0.09}_{-0.13}$	$0.02^{+0.01}_{-0.01}$	$0.46^{+0.20}_{-0.16}$	$0.19^{+0.31}_{-0.17}$
K2-277-exoE	$0.42^{+0.08}_{-0.08}$	$3.72^{+0.62}_{-0.67}$	$36.8^{+5.6}_{-6.9}$	$4.83^{+0.74}_{-0.85}$	$48.7^{+4.5}_{-6.7}$	$4.25^{+5.32}_{-3.37}$	$0.31^{+0.33}_{-0.17}$	$0.45^{+0.09}_{-0.15}$	-	$0.49^{+0.16}_{-0.14}$	$0.02^{+0.14}_{-0.02}$
K408-exoE	$0.39^{+0.07}_{-0.06}$	$4.30^{+0.63}_{-0.58}$	$44.2^{+6.1}_{-5.8}$	$4.19^{+0.59}_{-0.59}$	$44.2^{+4.8}_{-6.2}$	$1.55^{+1.89}_{-1.19}$	$0.07^{+0.10}_{-0.04}$	$0.17^{+0.03}_{-0.08}$	-	$0.44^{+0.12}_{-0.10}$	$0.45^{+0.64}_{-0.36}$
HD1461-exoE	$0.61^{+0.10}_{-0.08}$	$3.88^{+0.52}_{-0.46}$	$43.8^{+5.8}_{-5.1}$	$5.97^{+0.89}_{-0.80}$	$44.7^{+5.2}_{-6.5}$	$0.33^{+0.69}_{-0.27}$	$0.05^{+0.04}_{-0.02}$	$0.07^{+0.02}_{-0.05}$	-	$0.51^{+0.14}_{-0.12}$	$0.06^{+0.08}_{-0.04}$
HD219828-exoE	$0.57^{+0.09}_{-0.09}$	$3.85^{+0.57}_{-0.55}$	$40.4^{+5.6}_{-5.6}$	$5.86^{+0.91}_{-0.85}$	$46.9^{+4.5}_{-6.2}$	$1.64^{+2.26}_{-1.37}$	$0.13^{+0.14}_{-0.07}$	$0.20^{+0.04}_{-0.11}$	-	$0.45^{+0.13}_{-0.11}$	$0.03^{+0.15}_{-0.02}$
Earth[a]	0.36	3.58	38.1	4.49	45.4	8.11	-	-	-	-	-

	Core composition (wt per cent) and CMF (wt per cent)				
	Fe	Ni	Si	S	CMF
K10-exoE	$90.4^{+2.1}_{-3.1}$	$5.5^{+0.1}_{-0.2}$	$0.2^{+0.2}_{-0.1}$	$3.9^{+3.5}_{-2.0}$	$0.0^{+9.4}_{-0.0}$
K21-exoE	$89.7^{+1.7}_{-7.8}$	$5.2^{+0.3}_{-0.8}$	$3.3^{+3.1}_{-2.3}$	$1.7^{+0.5}_{-0.4}$	$28.8^{+6.5}_{-15.8}$
K37-exoE	$93.4^{+0.0}_{-1.1}$	$5.7^{+0.0}_{-0.5}$	$0.9^{+1.1}_{-0.7}$	-	$11.9^{+15.0}_{-11.9}$
K68-exoE	$80.3^{+7.1}_{-6.3}$	$5.0^{+0.7}_{-0.7}$	$13.2^{+6.1}_{-6.5}$	$1.5^{+0.3}_{-0.2}$	$38.7^{+4.2}_{-4.4}$
K93-exoE	$90.6^{+1.1}_{-5.8}$	$5.5^{+0.2}_{-0.7}$	$2.1^{+2.3}_{-1.5}$	$1.8^{+0.6}_{-0.5}$	$26.9^{+7.1}_{-14.2}$
K96-exoE	$88.0^{+4.9}_{-6.7}$	$4.9^{+0.7}_{-0.6}$	$5.5^{+4.2}_{-3.5}$	$1.6^{+0.3}_{-0.3}$	$36.4^{+4.4}_{-6.7}$
K100-exoE	$85.2^{+7.0}_{-8.2}$	$5.4^{+0.4}_{-0.8}$	$7.3^{+5.2}_{-4.6}$	$2.1^{+0.4}_{-0.4}$	$33.7^{+5.0}_{-7.7}$
K131-exoE	$82.5^{+7.1}_{-6.1}$	$5.0^{+0.7}_{-0.7}$	$10.9^{+5.5}_{-5.8}$	$1.5^{+0.3}_{-0.2}$	$39.7^{+4.4}_{-4.7}$
K2-222-exoE	$89.3^{+2.0}_{-8.1}$	$5.1^{+0.4}_{-0.8}$	$3.6^{+3.2}_{-2.5}$	$1.9^{+0.5}_{-0.4}$	$29.4^{+5.7}_{-13.6}$
K2-277-exoE	$87.8^{+3.9}_{-8.3}$	$5.4^{+0.3}_{-0.7}$	$4.8^{+4.1}_{-3.1}$	$2.0^{+0.5}_{-0.5}$	$33.6^{+5.4}_{-10.8}$
K408-exoE	$84.1^{+8.5}_{-8.1}$	$4.6^{+0.8}_{-0.6}$	$9.4^{+6.1}_{-5.6}$	$1.9^{+0.4}_{-0.3}$	$34.1^{+4.7}_{-5.9}$
HD1461-exoE	$81.0^{+7.7}_{-6.7}$	$5.4^{+0.6}_{-0.7}$	$11.9^{+6.2}_{-6.4}$	$1.8^{+0.3}_{-0.3}$	$38.3^{+4.5}_{-4.8}$
HD219828-exoE	$84.5^{+8.1}_{-7.6}$	$5.3^{+0.5}_{-0.7}$	$8.5^{+5.4}_{-5.1}$	$1.8^{+0.3}_{-0.3}$	$35.9^{+4.9}_{-6.5}$
Earth[b]	87.5	5.3	5.2	1.9	32.5 ± 0.3

[a] Refer to McDonough & Sun (1995) and normalize the contents of the adopted six major oxides to 100 wt per cent.
[b] Refer to Wang et al. (2018) and normalize the contents of the adopted four elements in the core to 100 wt per cent.

This paper has been typeset from a TEX/LATEX file prepared by the author.